

USGS Award No. G20AP00018

Final Technical Report

Improving Estimates of Ground-Motion Site Response in the New Madrid and Wabash Valley Seismic Zones

N. Seth Carpenter¹, Ph.D. (PI)
Zhenming Wang¹, Ph.D. (Co-I)
Edward Woolery², Ph.D. (Co-I)

¹ Kentucky Geological Survey
University of Kentucky
228 MMRB
Lexington, KY 40506
Phone: 859-323-0563
Fax: 859-257-1147
seth.carpenter@uky.edu
zmwang@uky.edu

² Department of Earth and Environmental Sciences
University of Kentucky
101 Slone Building
Lexington, KY 40506
Phone: 859-257-3758
Fax: 859-323-1938
woolery@uky.edu

Project Period
January 1, 2020 – June 30, 2021

This material is based upon work supported by the U.S. Geological Survey under Grant No. G20AP00018. The views and conclusions contained in this document are those of the authors and should not be interpreted as representing the opinions or policies of the U.S. Geological Survey. Mention of trade names or commercial products does not constitute their endorsement by the U.S. Geological Survey.

Abstract

In current engineering practice, the site coefficient for design ground motion is determined by the level of incoming ground motion and time-weighted average of shear-wave velocity for the top 30m of soils (V_{s30}). V_{s30} has been shown to be an inadequate proxy for site amplification because it does not account for resonance effects, which can exert strong control on site response, particularly in the central and eastern U.S. due to large sediment-bedrock impedance contrasts. In this project, we evaluated the skill of site fundamental frequency, f_0 , the corresponding amplification, A_0 , and sediment-bedrock impedance ratio (IR) to characterize the primary characteristics of site responses at 12 seismic stations in the New Madrid (NMSZ) and Wabash Valley (WVSZ) seismic zones. The IR , A_0 and f_0 parameters were calculated from shear-wave velocity (V_s) profiles developed at each site using 1D linear and equivalent-linear and nonlinear site response analyses. V_s profiles were developed at each site from surface SH-wave reflection/refraction soundings. For the three thicker-soil sites (sediment column thickness > 100 m), we estimated the deeper V_s by inversion of earthquake HVSR curves using constraints determined from P-wave and SH-wave soundings. We also measured the A_0 and f_0 parameters from S-wave HVSR curves that we developed at each site. Our results support the findings of other recent studies that the primary linear site-response characteristics needed for engineering purposes can be quantified by the A_0 and f_0 parameters at most sites. A corollary of this result is that the pair of parameters--both A_0 and f_0 --is needed to account for site resonance, and a single parameter alone, e.g. f_0 , is insufficient. For sites over thick soil deposits, a linear site-response calculation may be needed because the largest amplifications are predicted to occur at frequencies greater than f_0 . We also found that A_0 and f_0 can be reliably estimated by simplified expressions for one-layer-over-bedrock scenarios. Our observations also support the observations made in our study area and elsewhere that S-wave HVSR can be used to measure linear f_0 . However, we found no clear relationship between the amplitude of the HVSR peak at f_0 and that predicted by linear, equivalent-linear, and nonlinear 1D site responses. Furthermore, we determined that the bedrock-sediment impedance ratio can be used to estimate A_0 through a power-law relationship. Further, through the equivalent-linear and nonlinear modeling, consistent with other studies we found that theoretical f_0 decreases with increasing peak ground-motion amplitudes. Thus, the utility of weak-motion HVSR to predict f_0 in cases of strong motion is limited.

Report

Introduction

Site response is the modification of ground-motion in terms of its duration, frequency content, and amplitude by the near-surface low velocity materials. Site response can cause not only additional damage to susceptible infrastructure and buildings during earthquakes, but also affect accuracy of ground-motion estimates. Classic examples of significant damage caused by site response include Mexico City during the 1985 Michoacán earthquake (M 8.1) (e.g., Seed et al., 1988) and the Marina District of San Francisco during the 1989 Loma Prieta earthquake (M 6.9) (e.g., Bonilla, 1991). Thus, site response has become one of major research areas in engineering seismology, in central and eastern United States in particular (e.g., Woolery et al., 2008). For example, as a part of the Next Generation Attenuation for Central and Eastern North-America project (NGA-East) (Goulet et al., 2017), site response was recommended for incorporation into the U.S. Geological Survey National Seismic Hazard Maps by the Geotechnical Working Group (Stewart et al., 2017; Hashash et al., 2017).

Currently, the primary parameter for quantifying site response is the time-averaged shear-wave velocity for the top 30m of surficial materials, V_{s30} . Recent studies (e.g., Hassani and Atkinson, 2016; 2017) indicate that CEUS ground motion models have reduced uncertainties when the site terms account for site effects due to structure deeper than the upper 30m. Therefore, determining the site response at key seismic stations is needed for accurate, regional seismic hazard assessment in the CEUS, particularly in the vicinity of the highest sources of seismic hazard including the New Madrid and Wabash Valley seismic zones and in thick sediment layers, such as the northern Mississippi Embayment (Fig. 1).

In support of these recent studies, Fig. 1b shows shear wave velocity (V_s) structures derived from surface reflections/refractions and downhole tests at four sites along the Ohio and Mississippi Rivers (Fig. 1a). V_{s30} s were calculated for the sites and used to assign the NEHRP site classes. As shown in Figure 1b, all four sites are classified as **D** based on the V_{s30} values, even though the V_s structures, the depths to bedrock in particular, are significantly different, from ~20 m to ~600 m. Figure 2 shows spectral amplification functions derived from 1-D equivalent linear model, SHAKE91 (Idriss and Sun, 1992) for the four sites. Figure 2 shows that site responses (i.e., the peak frequencies and ratios) are quite different, particularly the base mode frequencies. In other words, site responses are significantly different for the four sites. Thus, V_{s30} is not an appropriate parameter to quantify site response for the New Madrid and Wabash Valley areas.

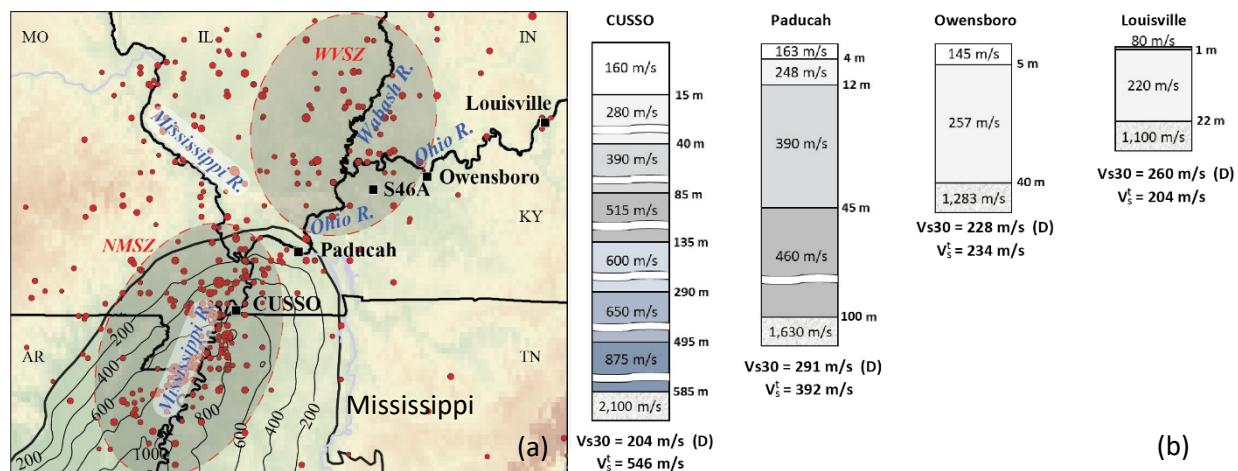


Figure 1. Study area and locations of V_s profiles (a) and V_s profiles at four sites along the Ohio and Mississippi Rivers (b). Time-weighted average shear-wave velocities from the surface to 30m (V_{s30} ; with the corresponding NEHRP site class), and to bedrock (V_s^t) are shown.

For a single sediment layer on elastic bedrock subjected to a vertical-incidence SH-wave, Haskell (1960) found that the un-damped resonance frequencies are

$$f'_n = \frac{V_s(2n + 1)}{4H}, \quad n = 0, 1, 2, 3, \dots \quad (1)$$

where, V_s , and H are average sediment shear-wave velocity and total sediment thickness, respectively. As shown by Dobry et al. (2000), at the fundamental resonance frequency (i.e., the inverse of the site period, T_0), $f'_0 = V_s/(4H)$, the peak amplification of response spectra between soil site and nearby rock site can be approximated as

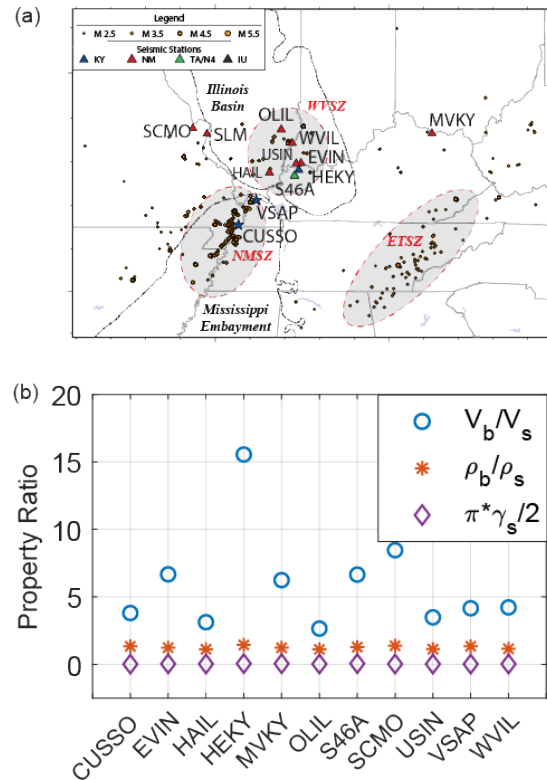
$$\tilde{A}_0 \approx \frac{1}{\left(\frac{\rho_s V_s}{\rho_b V_b}\right) + \frac{\pi \gamma_s}{2}} \quad (2)$$

where ρ_b and ρ_s , are densities of bedrock and sediment overburden, V_b is the V_s of rock. $(\rho_s V_s)/(\rho_b V_b)$ is the sediment/rock impedance ratio, and γ_s is the shear-wave the damping ratio. Sediment-property parameters in equation 2 are calculated as thickness averages, except for V_s , which is the time-weighted average. Carpenter et al. (2020) evaluated these parameters using velocity profiles at the seismic stations shown in Figure 2.

Figure 2. (a) Figure 5. Seismic stations, colored by network code, and the epicenters of earthquakes used in the Carpenter et al. (2020) study. The Wabash Valley (WBSZ), New Madrid (NMSZ), and eastern Tennessee (ETSZ) seismic zones are delineated by the shaded ellipses. (b) Values of the terms in equation (2) calculated from average, one-layer-over-bedrock velocity structures determined at the seismic stations in (a).

As shown in Figure 1b, there are significant velocity contrasts between bedrock, with V_s greater than 2,100 m/s and sediments with V_s less than 875 m/s (sediment-column average velocities are less than 546 m/s). This velocity contrast between the sediments and bedrock is extant throughout the New Madrid and Wabash Valley Seismic Zones (e.g., Street et al., 2001, 2004; Woolery et al., 2009, 2012).

Equation 2 estimates amplification at f_0 , A_0 , from the sediment/rock impedance ratio and the S-wave damping ratio of sediment. Sediment densities are in the range of 1.5 to 2.0 g/cm³, and the density of rock is in the range of 2.4 to 2.7 g/cm³. The sediment V_s normally varies from 100 to 800 m/s, and bedrock V_s varies from 1,000 to 2,000 m/s. These result in the sediment/rock impedance contrast having a typical range of 0.028 to 0.664. The damping ratio of sediment normally falls in the range of



0.01 to 0.10. Figure 2 shows the relative influences of the property ratios given as terms in equation 2 on \tilde{A}_0 and demonstrates that the velocity ratio, and thus the impedance ratio, exerts the greatest control on amplification at f_0 .

The parameter f_0 has been proposed to be of primary importance in accounting for site response (e.g., Cadet et al., 2010; Hassani and Atkinson, 2016, 2017). As shown by Hassani and Atkinson (2016, 2017), using f_0 as the primary parameter improves estimates of site response (i.e., reduction of site variability). As also shown by Hassani and Atkinson (2017), however, f_0 alone is not enough to account for the variability of site response. Hassani and Atkinson (2017) further suggested using both f_0 and V_s30 for site response model. However, as shown in Figure 1, V_s30 is inadequate to capture site response, which involves resonance. In addition, as shown in equations (1) and (2), f_0 does not capture the other important part of site response, i.e. the amplification factor. As illustrated in Figure 2, the amplification at f_0 is most strongly influenced by the sediment/rock impedance ratio. Thus, both f_0 and sediment/rock impedance contrast or A_0 may serve as primarily parameters for improving estimates of site response.

Carpenter et al. (2018a) demonstrated that mean earthquake shear-wave horizontal-to-vertical spectral ratios (HVSR) using the transverse-component approximate the empirical transfer functions at the bedrock-penetrating borehole observatories in the Mississippi Embayment, CUSSO and VSAP. The approximation degrades, however, for frequencies above approximately the 5th resonance mode due to vertical-component amplification. Therefore, lower-frequency S-wave HVSR is useful for not only estimating site fundamental frequencies, but also for approximating A_0 .

The chief purposes of this project were therefore two-fold. First, primary site response factors f_0 and A_0 were estimated at 12 temporary or permanent seismic stations in the New Madrid and Wabash Valley seismic zones. This estimation involved determining V_s structures at each station by surface SH-wave reflection/refraction soundings and inversion of S-wave HVSR at the three deep-soil (>100 m) sites. The skillfulness of f_0 and A_0 to characterize site response was then evaluated using 1D response simulations. Second, the skill of S-wave HVSR to estimate f_0 and A_0 was also assessed by comparing measurements of the first peaks from site S-wave HVSR curves with the 1D simulations.

Methods

Site Selection

We selected 12 broadband or strong-motion seismic stations situated in or near the Wabash Valley and New Madrid seismic zones for the project sites. The candidate stations considered for this project (Fig. 3) are on a range of site conditions from bedrock outcrop and shallow (meters) to thick (100s of meters) sediment, and from softer (younger) to stiffer (older) sediments. These stations traverse the New Madrid and Wabash Valley seismic zones, and for the final selections priority was given to N4 and NM network stations; other stations – e.g. temporary EarthScope TA and FA stations – were selected to sample various site conditions or geologies.

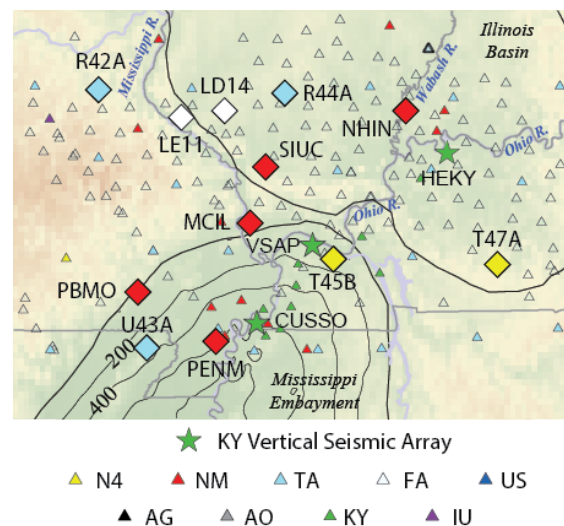


Figure 3. Broadband and strong-motion seismic stations operating in the Wabash Valley and New Madrid seismic zones, colored by network code (<http://www.fdsn.org/networks/>). The stations selected for this study are shown as diamonds. Vertical seismic arrays in the project area are shown as stars.

The deep, bedrock-penetrating borehole sites, CUSSO and VSAP (Woolery et al., 2016; Carpenter et al. 2018a), are in the project area and provide empirical S-wave transfer functions and V_s structure control to depths up to almost 600 m in the sediments of the upper Mississippi embayment.

Selecting the 12 stations required assessing the number of S-wave recordings suitable for HVSr analysis. We used ObsPy (Beyreuther et al., 2011) and ObsPlus (Chambers et al., 2021) to acquire and process earthquake recordings available at IRIS DMC (<http://www.ds.iris.edu/ds/nodes/dmc/>). For a subset of the stations shown in Figure 3, we downloaded three-component waveforms for all earthquakes in the USGS PDE catalog of magnitude 2.5 and greater within 3° of each station. The time windows of the downloaded recordings started at least 30 s prior to the predicted P-wave arrival time and extended 60 s after the predicted S-wave arrival time. We manually inspected all recordings and rejected those that included instrument glitches or high-amplitude noise transients in the signal or noise windows.

Carpenter et al. (2018a) obtained stable, mean S-wave HVSr curves from 10 events with signal-to-noise ratios (SNR) of 1.5 and greater for all frequencies on both the transverse and vertical components. Hassani and Atkinson (2017) required even fewer recordings, a minimum of three, to obtain reliable HVSr curves. Following Carpenter et al. (2020), for this project we required at least three observations at each frequency of interest, where only those observations having SNRs of 2.5 or greater were considered. Table 1 lists the stations selected for this investigation.

Table 1. Seismic stations included in this investigation

Network	Station	Latitude (°N)	Longitude (°E)	Offset (m)
XO	LD14	38.1305	-89.6138	80
XO	LE11	38.0657	-90.0121	96
NM	MCIL	37.2954	-89.5058	123
NM	NHIN	38.1305	-87.9361	14
NM	PBMO	36.7785	-90.4297	0
NM	PENM	36.4497	-89.6282	105
TA	R42A	38.2804	-90.7944	173
TA	R44A	38.2475	-89.0809	88
NM	SIUC	37.7085	-89.2400	0
N4	T45B	37.0159	-88.6459	8
N4	T47A	36.9881	-87.1055	3
TA	U43A	36.3693	-90.4057	212

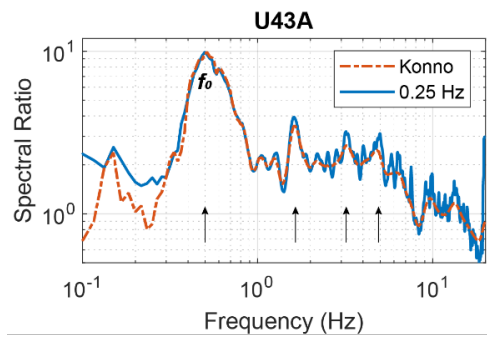
S-wave HVSr Analysis

To process the local and regional earthquake recordings, we largely followed the processing procedures used in the Carpenter et al. (2018a; 2020) studies. First the Fourier spectra are calculated from the windowed, de-trended, de-measured, and tapered (5 percent of window-length cosine tapers) waveforms. Time windows began 1.0 s prior to the direct-S arrival. To capture multiple reverberations in the sediment columns, we used window lengths at least $10/f_0$ (similar to the SESAME standards for HVSr processing (SESAME project, 2004)). For all sites except PENM, the S-wave windows were 30.0 s. At PENM, which overlies the thickest column of unlithified sediments, we the window was 35.7 s.

Instrument responses were removed from these preprocessed, windowed waveforms, and the amplitude spectra were calculated. Amplitude spectra were then smoothed with running Hanning windows with site-dependent lengths of $f_0/2$ Hz.

We used a fixed-length smoothing window rather than the logarithmically spaced Konno-Omachi algorithm (Konno and Ohmachi, 1998) for two reasons. First, the Carpenter et al. (2020) study, which reported a linear relationship between the theoretical site response at f_0 and the magnitude of the first peak measured from S-wave HVSR curves, also used window lengths of $f_0/2$ Hz. The observations from this project could improve that relationship, which suggests that linear site amplification can be estimated from S-wave HVSR. Thus adopting a similar processing procedure is important for dataset compatibility. Second, Konno-Omachi smoothing tends to reduce important HVSR peaks at frequencies greater than f_0 , which are useful for estimating V_s in the deeper layers at sites in the Mississippi embayment. Figure 5 compares mean S-wave HVSRs determined from spectra smoothed with fixed-length windows with those determined from Konno-Omachi smoothing (bandwidth = 40).

Figure 4. Mean S-wave HVSRs developed at site U43A developed from amplitude spectra smoothed using Konno-Omachi smoothing (Konno) and using fixed-window length of $f_0/2$ Hz (0.25 Hz). Prominent peaks in the spectral ratio, most of which are muted by Konno-Omachi (bandwidth=40) smoothing are indicated by arrows.



We excluded unreliable signal at each frequency via signal-to-noise ratios calculated in the frequency domain. Noise amplitude spectra were estimated from the Fourier spectra of 30 s of pre-P-wave noise. SNRs were calculated by spectral division and used to filter out low-quality spectral estimates. We retained only S-wave spectra at frequencies for which both the transverse and vertical components had SNRs of at least 2.5. Figure 5 presents an example of processing a single earthquake recording at U43A from windowing the waveforms to selection of the usable parts of the HVSR curve.

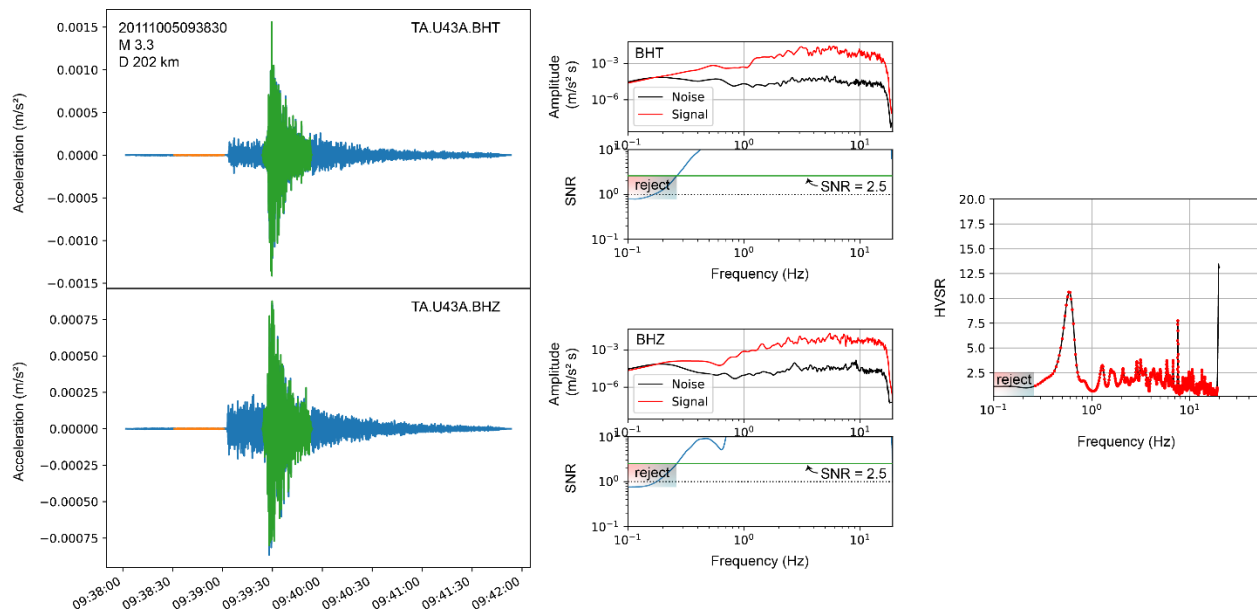


Figure 5. Example of the HVSR data-processing workflow using the recordings of an M 3.3 earthquake at TA.U43A, 202 km from the station. After preprocessing the recordings, noise (orange) and signal (green) windows are taken on the transverse- (BHT) and vertical-component (BHZ) recordings (left column). Amplitude spectra are calculated for both noise and signal windows and signal-to-noise ratios (SNR) are formed for both components (middle column). The HVSR spectral ratio for this recording is calculated from the spectral division of BHT by BHZ, but only for frequencies with SNR 2.5 or greater (right column).

Final, site HVSR curves (e.g., Figure 4) were calculated by taking the mean of the individual-event spectral ratios at each frequency. The fundamental mode frequency and spectral ratio were measured from the mean S-wave HVSR curves using the procedure described in Carpenter et al. (2020): We picked the first clear peaks using the MATLAB function FINDPEAKS, stipulating that peaks have a prominence of at least 1.0. In other words, if a peak's height above either of the adjacent troughs was less than 1.0, it was not considered. We searched for the first peak within the primary band of engineering interest, from 0.1 to 10 Hz.

Shear-wave Velocity Profile Development

Reflection/refraction profiling

Surface SH-wave reflection/refraction methods have been widely used to obtain shear-wave velocity profiles in the region (e.g., Street et al., 1997a, 2001; Williams et al., 2003; Williams et al., 2000; Woolery et al., 2009). These researchers reported that it is difficult to obtain direct shear-wave velocity measurements using these techniques for depths from 200 to 300 m in the Mississippi Embayment, without additional constraints. In addition, Street et al. (1997a, 2001) suggested that most S-wave velocity variation occurs within the upper 200 m. Consequently, for the sites that overly deep soils we combined direct SH-wave refraction-based measurement methods used to define the velocity model for the upper parts of the velocity structure with constrains obtained from P-wave walkaway reflection soundings to estimate V_s of the deeper layers through inversion of the site S-wave HVSR curves.

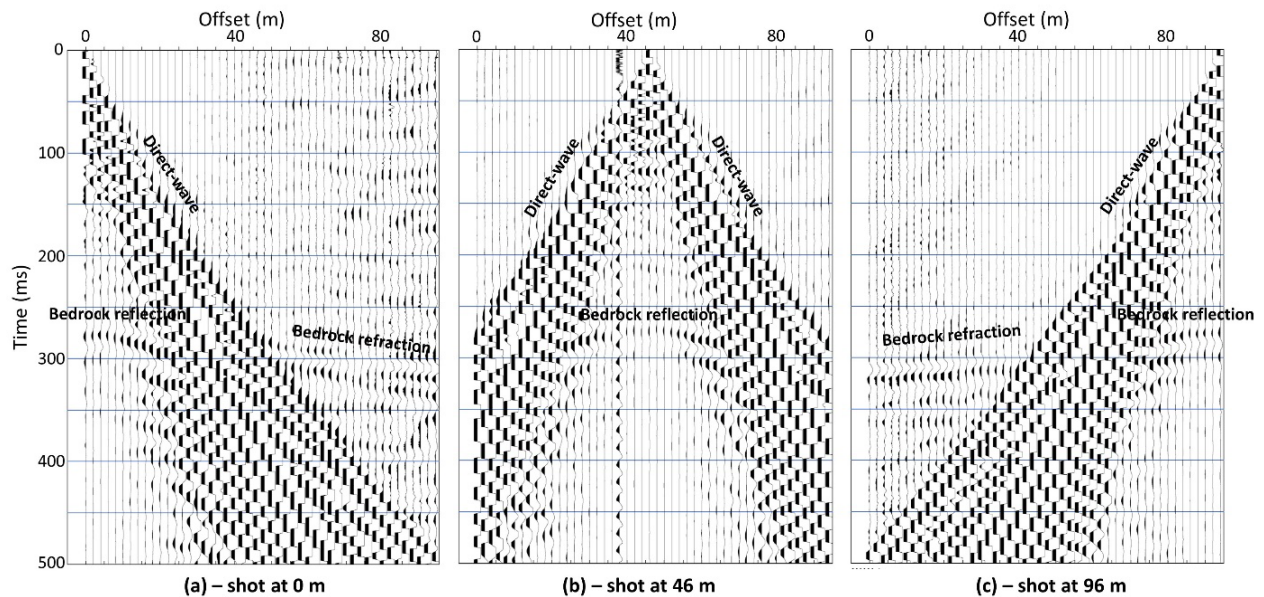


Figure 6. SH-wave seismic reflection/refraction data collected at site MCIL with a geophone interval of 2 m. (a) – the shot point at 0 m (first geophone); (b) - the shot point at 46 m (the 24th geophone); and (c) the shot point at 96 m (the 48th geophone).

SH-wave reflection/refraction data was acquired with 24 or 48 (depending on site constraints) inline, 30 Hz, horizontally polarized geophones spaced at intervals of 1, 2, or 4 m depending on the assumed thickness of soils at the stations, with shot points at the zero offsets, the midpoint, and others positions relative to the geophone array. Seismograms were acquired at a sampling interval of 0.25 ms. The energy source was an 8 lb or 12 lb hammer striking a steel I-beam oriented perpendicular to the orientation of the geophone array. The SH-wave data were processed and interpreted SeisImager/2D (Geometrics, 2009). Figure 6 shows the SH-wave seismic reflection/refraction recordings collected at site MCIL with geophone interval of 2 m. The interpreted shear-wave velocity and depth model from the SH-wave refraction at site MCIL was shown in Figure 7.

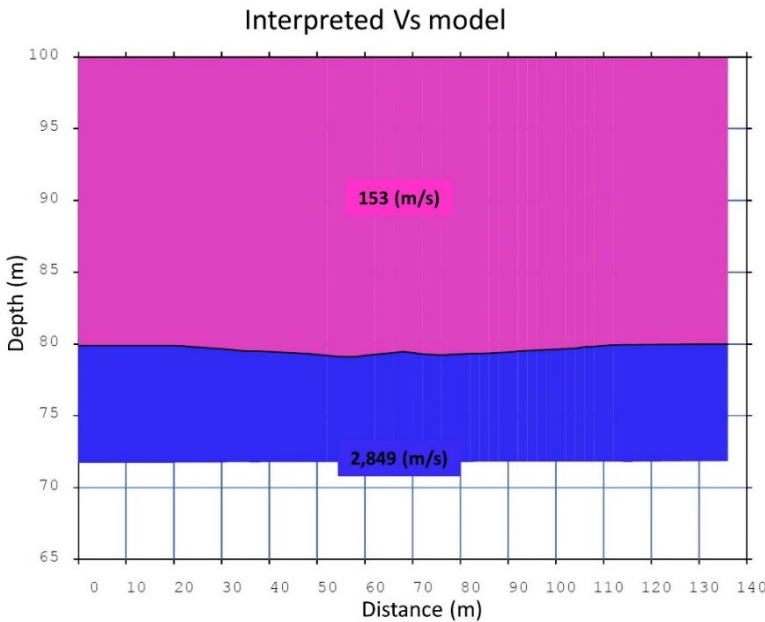


Figure 7. *Interpreted shear-wave velocity and depth model from the SH-wave refraction at site MCIL.*

Sites having deeper stratigraphic tops where critical distances were too large to practically measure with seismic refractions utilized the seismic-reflection walkaway technique. The walkaway method, sometimes called seismic “drilling,” derives stratigraphic impedance boundary depths by moving a seismic energy source to increasingly larger offsets from a fixed array of geophones and splicing the individual shot seismogram panels into a

continuous, length-consistent, composite seismogram useful for noise and velocity analyses. The two-way zero-offset travel time and stacking velocity for each reflection were estimated using an interactive hyperbolic curve-fitting program, and the interval velocity and thickness for each formation determined by an algorithm based on Dix’s (1955) equation. Woolery and Wang (2010) compared stratigraphic elevations derived from a P-wave walkaway test and those interpreted from an adjacent 585-m borehole log and found no more than 2.5% variation in their comparison of stratigraphic horizons between the base of the Quaternary sediment at 48 m depth and the top of the Paleozoic bedrock at 585 m depth.

Walkaway data were recorded with a 24 bit, 48 channel, instantaneous floating-point, engineering seismograph, and a receiver array of two inline spreads with 24 single-point 40-Hz vertical geophones spaced at a 2 or 4 m interval. The P-wave energy source was five vertical strikes per shot point of a 4.5 kg hammer onto a 15 cm² × 2.5 cm thick hardened aluminum plate. The sample interval was 0.25 ms for all recordings, and record lengths were typically 1.024 s. The signal-to-noise ratio for the soundings varied in quality but was generally controlled by the cultural environment. Minimal signal enhancement procedures were applied to the data, generally limited to band-pass filtering (e.g., between 35 and 140 Hz) and automatic gain control (e.g., 100 ms window). Table 2 lists the survey locations and acquisition parameters used.

Table 2. Reflection/refraction survey locations and configuration parameters.

Site	Latitude (°N)	Longitude (°E)	Offset (m)	SH-win (s)	dg_SH (m)	Ng_S H	P-win (s)	dg_P (m)	Ng_P
LD14	-89.6140	38.1312	80	1.024	1	48	-	-	-
LE11	-90.0131	38.0661	96	1.024	1	48	-	-	-
MCIL	-89.5061	37.2943	123	1.024	2	48	-	-	-
NHIN	-87.9363	38.1304	14	1.024	1	48	-	-	-
PBMO	-90.4297	36.7785	0	0.512	1	24	-	-	-
PENM	-89.6270	36.4497	105	2.048	4	48	1.024	4	48
R42A	-90.7926	38.2798	173	1.024	1	24	-	-	-
R44A	-89.0819	38.2476	88	1.024	2	48	-	-	-
SIUC	-89.2400	37.7085	0	1.024	2	48	-	-	-
T45B	-88.6460	37.0158	8	1.024	2	48	1.024	2	48
T47A	-87.1056	36.9881	3	0.512	1	24	-	-	-
U43A	-90.4080	36.3697	212	2.048	2	48	1.024	2	48

Offset – distance from seismic station to the reflection/refraction survey’s midpoint; *SH-win* – SH-wave acquisition time window; *dg_SH* – SH-wave geophone spacing; *Ng_SH* – Number of SH-wave geophones; *P-win* – P-wave acquisition time window; *dg_P* – P-wave geophone spacing; *Ng_P* – Number of P-wave geophones.

S-wave HVSR inversion

For the thicker-soil (sediment thickness > 100 m) sites in the Mississippi embayment—i.e., PENM, T45B, and U43A— V_s of the deeper layers was estimated through fitting S-wave HVSR curves with theoretical SH-wave and P-wave 1D site response functions. Studies in the past decade have shown that HVSR derived from earthquake seismograms can be used to estimate shear-wave velocity structure (Kawase et al., 2011; Nagashima et al., 2014; Rong et al., 2016). Towards an alternative, simpler approach that does not require the vertical transfer function, Carpenter et al. (2018b; 2019) found that mean, weak-motion, local- and regional-earthquake HVSR curves can be used to resolve shear-wave velocity structures that are consistent with published velocity models. However, due to the presence of converted phases within the vertical-component S-wave window, the similarity between S-wave HVSR and the SH-wave transfer function degrades at high frequencies. In particular, vertical-component amplification of P-waves converted from SV-waves at the sediment-bedrock interface (e.g., Parolai and Richwalski, 2004; Rong et al., 2017; Carpenter et al., 2018a) reduces HVSR for frequencies above a site-dependent maximum frequency, f_{max} , which is approximately the fifth resonance mode (approximately nine times f_0). In the Carpenter et al. (2018b; 2019) studies, velocity structures—free parameters for each layer were V_s and thickness—were determined by perturbing the starting earth model until the misfit between the S-wave HVSR curves and the predicted 1D SH-wave response up to the fifth resonance mode is minimized.

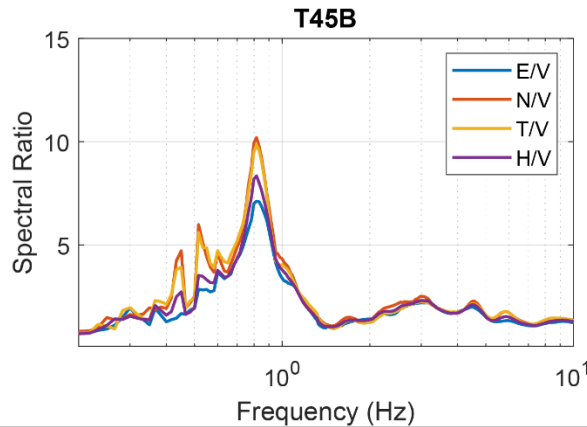
In this investigation we found that both the P-wave and SH-wave transfer functions are needed to resolve reasonable velocity structures at the embayment sites. In contrast to the S-wave HVSR curves determined for the sites in the Carpenter et al. (2018b; 2019) studies, where the peak magnitude in the spectral ratio occurred at frequencies higher than the sites’ f_{0S} , i.e., $f_{peak} > f_0$, at PENM, T45B, and U43A, higher modes are less energetically expressed on the S-wave HVSR curves, and $f_{peak} = f_0$ on HVSR. Fitting these curves with SH-wave transfer functions required unrealistically fast, shallow layers underlain by strong velocity inversions, unobserved by the reflection surveys. However, inclusion of the P-wave

responses in the velocity-structure inversions, consistent with the Kawase et al. (2011) diffuse-field theory framework, returned velocity structures consistent with those derived at nearby stations.

According to diffuse-field theory of multiple, scattered earthquake body waves, HVSR is related to the horizontal- and vertical-component 1D transfer functions by the following expression.

$$HVSR = \sqrt{\frac{2\alpha |TF_S|}{\beta |TF_P|}} \quad (3)$$

where TF_S and TF_P are the 1D S-wave (horizontal) and P-wave (vertical) transfer functions, respectively, and α and β are the P- and S-wave velocities in bedrock, respectively. The factor of 2 in equation 3 implies that body-wave energy density is equally partitioned onto both horizontal components. Our S-wave HVSR processing used transverse-component S-wave recordings, which may not constitute equally partitioned amplitudes in the S-wave windows. As the various HVSRs shown in Figure 8 for T45B illustrate, the mean spectral ratios depend on the horizontal components used to form the curves, particularly at f_0 . Figure 8 also shows that the geometric mean of the unrotated amplitude spectra, herein called the H-component spectrum, is approximately the average of the maximum and minimum spectral ratios. Thus, we used HVSRs determined from the H-components to form the S-wave HVSR curves, eHVSR, for inversion under the assumption that they more likely reflect the spectral ratios from



an equipartitioned wavefield. In this case, the one-directional representation of the diffuse-field HVSR, expressed in equation 4, is appropriate (Matsushima et al., 2014).

Figure 8. Various mean horizontal-component HVSRs determined at T45B: E/V – east-to-vertical S-wave HVSR; N/V – north-to-vertical S-wave HVSR; T/V – transverse-to-vertical S-wave HVSR; H/V – mean horizontal-to-vertical S-wave HVSR, where the mean is calculated as the geometric mean of the unrotated horizontal-component amplitude spectra.

$$eHVSR = \sqrt{\frac{\alpha |TF_S|}{\beta |TF_P|}} \quad (4)$$

We used mean eHVSR curves at the embayment sites to estimate the deeper S-wave velocity structure using equation 4 through a guided Monte Carlo procedure. Similar to Rong et al. (2017) and Carpenter et al. (2018a), we modeled the spectral ratios in equation 4 as 1D responses at the surface of S-waves and of P-waves, assuming vertical incidences. As in Carpenter et al., 2018 and 2020, we used the Thompson-Haskell propagator-matrix formulation (Haskell, 1960) to calculate the forward models (i.e., body-wave responses) at each iteration in the inversion, where the misfit between the left and right sides of equation 4 is to be minimized. In our procedure, the sediment P-wave velocity structures—P-wave velocities, V_p , and layer thicknesses, h —were held fixed since they were determined from the reflection surveys. Free parameters were V_s , densities (ρ), and effective S-wave and P-wave quality

factors, Q_s and Q_p respectively. The layer V_s estimated through SH-wave refraction profiling were held fixed. Bedrock densities and velocities (α and β) and quality factors were also estimated.

As in the Carpenter et al. (2020) study, we estimated ρ and Q_s layer properties from layer V_s (for both fixed and free V_s) using published statistical relationships. The $Q_s(V_s)$ relationships we used came from equations 20, 21, and 22 in Wang et al. (1994) and models 1 and 3 in Campbell (2009). We calculated Q_s as the mean of the values predicted from each of these mathematical models. Following the standard approach commonly employed in 1D site-response software (e.g., STRATA; Kottke and Rathje, 2008), the effective quality factors are assumed to include the effects of frequency-independent intrinsic attenuation and frequency-dependent scattering. We estimated ρ from V_s using the relationship in Boore et al. (2016). We also constrained bedrock V_p to be no more than 1.74 times V_s , consistent with the V_p - V_s ratio of bedrock in the embayment determined in Langston (2003).

Because the properties of the shallowest layers were determined through processing the reflection/refraction survey data, we focused on constraining the properties of the deeper layers through the inversion of the eHVSr curves. Thus, we resampled the curves logarithmically to give the long-period parts of the empirical spectral ratios more influence, which, as demonstrated in Peng et al. (2020) can be used to resolve deeper layer properties. We executed the Monte Carlo inversions using the open-source software developed by Bignardi et al. (2016). We modified the software to use our forward-model calculator, to estimate ρ and Q_s from V_s , to allow fixing layer thicknesses as well as total-sediment thickness, and to scale the ratio of S-wave-to-P-wave surface responses by $\sqrt{\alpha/\beta}$ as in equation 4.

The starting model consisted of layer V_p and V_s derived from the reflection/refraction soundings. The S-wave velocities of the deeper layers in the starting model were initially uniform and estimated from the observed f_0 from S-wave HVSr using the approach described in Peng et al. (2020): assuming vertical SH-wave incidence in a 1D near-surface earth model, f_0 can be calculated from equation 1 as

$$f_0 = \frac{1}{4 * \sum_i h_i / V_{S_i}} \quad (5)$$

where h_i are the layer thicknesses and V_{S_i} are layer S-wave velocities. Thus, using the observed f_0 , the layer thicknesses to bedrock, and the measured (shallow) V_s , equation 5 can be used to estimate the average V_s of the deeper layers.

Carpenter et al. (2019) found that layer thicknesses are necessary to constrain reasonable layer velocities. Thus, we only modeled scenarios in with fixed layer thicknesses. We did evaluate other starting V_s scenarios, including allowing V_s to be free for all layers and fixing the top-layer V_s only. Our simulations supported the experience of Carpenter et al. (2019) that unreasonable shallower velocity structures—i.e., which differ substantially from those determined from the reflection/refraction surveys—can result. Thus, we fixed the velocities of the layers determined from the reflection/refraction surveys. Though this approach revealed reasonable V_s models, only executing a single inversion strategy limited our ability to assess model uncertainties. Nevertheless, the V_s models developed for T45B and U43A did not vary for each trial, suggesting that these models are well-constrained. The large variability in the models resolved for PENM suggests the opposite. However, as shown below, the comparisons with the best-fitting velocity model and corresponding site responses for this site with other nearby sites are favorable.

To calculate the terms in equation 4 for each iteration, the free parameters V_{S_i} , Q_{S_i} , Q_{P_i} , α , and β were perturbed by a random amount uniformly distributed from 0% to 10% of the parameter values in the previous iteration. The objective function to be minimized was

$$m = w_A * \sum \left(eHVSR - \sqrt{\alpha/\beta} |TF_S|/|TF_P| \right)^2 + \quad (6)$$

$$w_S * \sum \left(\frac{d[eHVSR]}{df} - \frac{d[|TF_S|/|TF_P|]}{df} \right)^2$$

where w_A and w_S , i.e., weights of the amplitude and slope misfit, respectively, were 0.999 and 0.001, respectively. Perturbations that did not improve the fit to the observed eHVSR were ignored. For each of the embayment sites, at least five trials of 10,000 iterations each were conducted to mitigate the possibility of the final model resulting from trapped in local minima. More than five trials were conducted for sites where convergence histories varied strongly across the trials or when the best-fitting model was obtained at large numbers of iterations. In this study, the only site for which more than five trials were conducted was PENM.

1D Linear, Equivalent-linear, and Nonlinear Analyses

We calculated 1D linear response for vertically incident SH-waves using the Thompson-Haskell propagator-matrix formulation (Haskell, 1960) and the near-surface earth models developed in this project. Carpenter et al., (2018a) demonstrated that the 1D full-resonance responses calculated by the Thomson-Haskell matrix method are reasonable for two sites in this study area—namely CUSSO and VSAP—by comparing the theoretical responses with borehole surface-to-bedrock spectral ratios. Carpenter et al. (2020) demonstrated that the same formulation was appropriate to evaluate 1D site responses at other CEUS sites. Thus, we employed the same methodology in this study. We incorporated viscoelastic effects in the site response calculations, modeled as Kelvin-Voigt solids, through complex shear moduli in each layer (e.g., Joyner et al., 1976), which assumes frequency-independent damping (as is the case in common site-response codes such as SHAKE91 and STRATA).

1D dynamic site response modeling program, DEEPSOIL (V7.0) (Hashash et al., 2020), was used for equivalent-linear and nonlinear site-response analyses for this project. Input parameters for the analyses include soil shear-wave velocity, thickness, density, shear modulus, and damping reduction curves. The shear-wave velocities and thicknesses of soils and bedrock were derived from the surface seismic reflection/refraction and HVSR analyses in this study. The densities (ρ : in g/cm³) were estimated from shear-wave velocities, V_S (in km/s), using the relationships of Boore (2016):

$$\rho = 1 + \frac{1.53V_S^{0.85}}{0.35+1.889V_S^{1.7}}, \quad (7)$$

for $V_S < 0.30$ km/s, and:

$$\rho = 1.74 \times (0.9409 + 2.0947V_S - 0.8206V_S^2 + 0.2683V_S^3 - 0.0251V_S^4)^{0.25}, \quad (8)$$

for $0.30 \text{ km/s} < V_S < 3.55 \text{ km/s}$. We used the statistical relationship between quality factor (Q_S) and V_S in m/s from Wang et al. (1994):

$$Q_S = 0.08V_S + 6.99, \quad (9)$$

and Campbell (2009),

$$Q_S = 0.0276V_S + 7.17, \quad (10)$$

to estimate layer minimum damping values ($1/2Q_s$). The shear modulus and damping reduction curves were selected from the built-in database in the DEEPSOIL.

The input ground motions include one weak-motion recorded at the vertical strong-motion array in Paducah (VSAP) from the 2008 southern Illinois earthquake (Mw 5.2), two synthetic strong motions from the New Madrid Mw 7.2 earthquake and Wabash Valley Mw 6.3 (Wang et al., 2008), one strong motion from the 1989 Loma Prieta, California, earthquake (Mw 6.9), one from the 1994 Northridge, California, earthquake (Mw 6.7), one from the 1999 Chi-Chi, Taiwan, earthquake (Mw 7.7), and one from the 2008 Wenchuan, China, earthquake (Mw 7.9). Figure 9 shows the weak motion from the 2008 southern Illinois earthquake (a), synthetic strong motion from the Wabash Valley earthquake (b), and strong motion the 1994 Northridge earthquake (c).

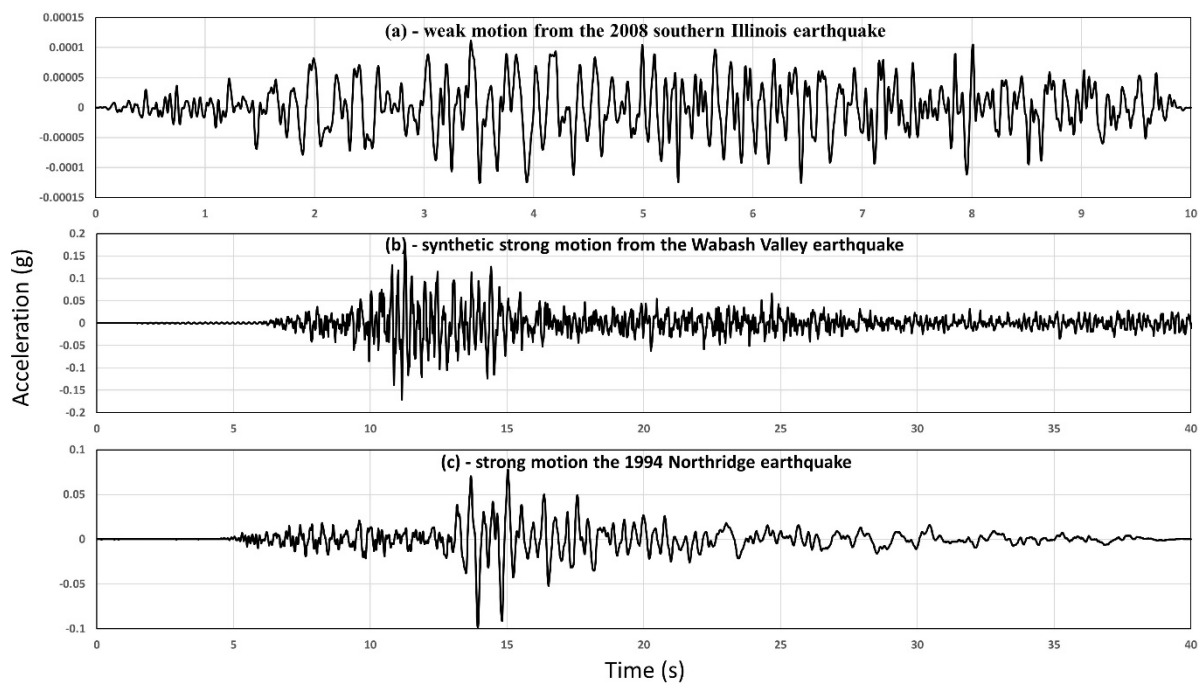


Figure 9. Weak motion from the 2008 southern Illinois earthquake (a), synthetic strong motion from the Wabash Valley earthquake (b), and strong motion from the 1994 Northridge earthquake.

Figure 10 shows the spectral amplifications calculated for sites LD11 and PENM with the input strong motion from the 1994 Northridge earthquake. As demonstrated in Figure 10, we determined the fundamental site frequency (f_0) and its associated amplification (A_0) from the spectral amplification curves.

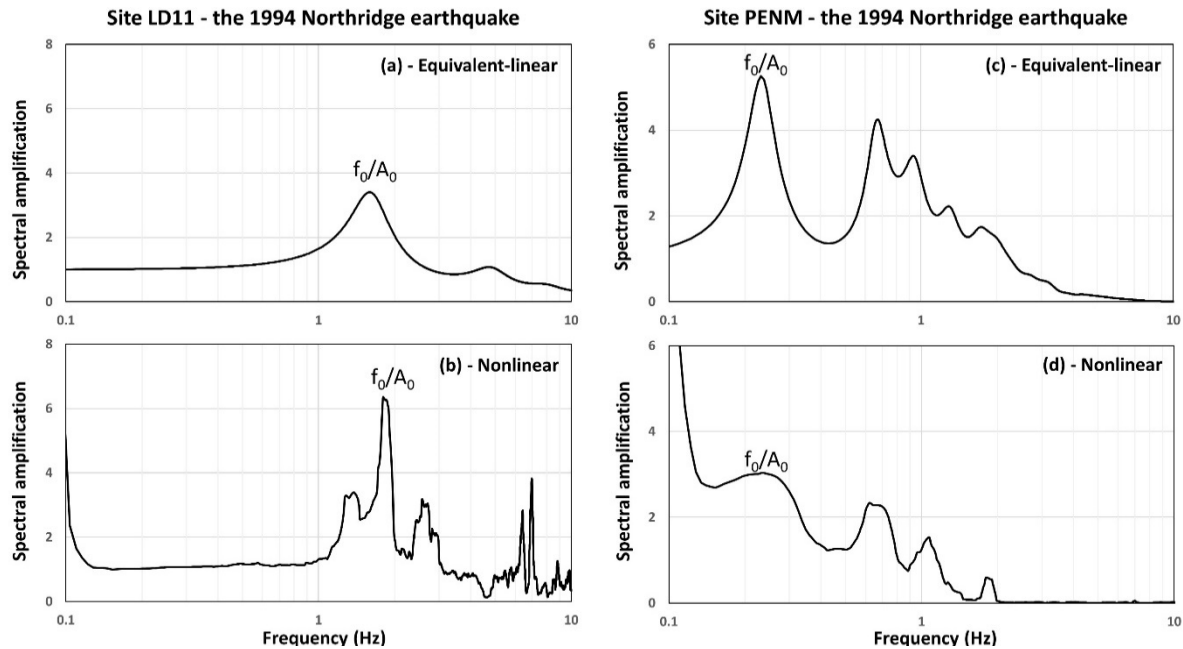


Figure 10. Equivalent-linear and nonlinear spectral amplifications calculated for sites LD11 and PENM with the input strong motion from the 1994 Northridge earthquake.

Results

S-wave HVSR

Table 3 lists the number of magnitude 2.5 and greater earthquakes used to calculate the mean S-wave HVSRs at each site and the maximum peak ground acceleration (PGA) in the dataset. The maximum PGA are all weak (< 50 gal), and therefore nonlinear ground-motions are not expected to have occurred in this dataset. Table 3 also lists S-wave time-series processing parameters used for windowing around S-wave arrivals at each station and those parameters used for HVSR processing. The f_0 measured from the mean S-wave curves are also shown. The distributions of local and regional earthquakes used for S-wave HVSR analyses are shown in Figure 11.

Table 3. S-wave HVSR data set, processing parameters, and fundamental-mode parameters

Station	Neq	max. PGA (gal)	S-win (s)	f_{smooth} (Hz)	$f_{0,HV}$ (Hz)	$A_{0,HV}$
LD14	17	0.7	30.0	1.2	2.5	4.8
LE11	17	1.3	30.0	1.3	2.7	4.1
MCIL	51	2.3	30.0	1.0	2.0	15.4
NHIN	36	7.0	30.0	2.1	4.2	4.6
PBMO	51	4.8	30.0	2.1	4.3	5.4
PENM	51	11.3	35.7	0.14	0.28	9.8
R42A	20	1.3	30.0	2.5	5.0	4.4
R44A	18	1.2	30.0	2.7	5.4	7.6
SIUC	51	1.6	30.0	3.8	7.6	7.6
T45B	51	1.8	30.0	0.41	0.82	7.8
T47A	51	1.0	30.0	3.6	7.2	2.7
U43A	31	1.7	30.0	0.25	0.50	9.9

Neq – Number of earthquake recordings used; *max. PGA* – maximum acceleration in the recordings used; *S-win* – time-series window lengths used for spectral analyses; *f_{smooth}* – length of Hanning window used to smooth amplitude spectra; *f_{0,HV}* – fundamental site frequency estimated from HVSR analysis; *A_{0,HV}* – spectral ratio measured at *f_{0,HV}* on the S-wave HVSR curves.

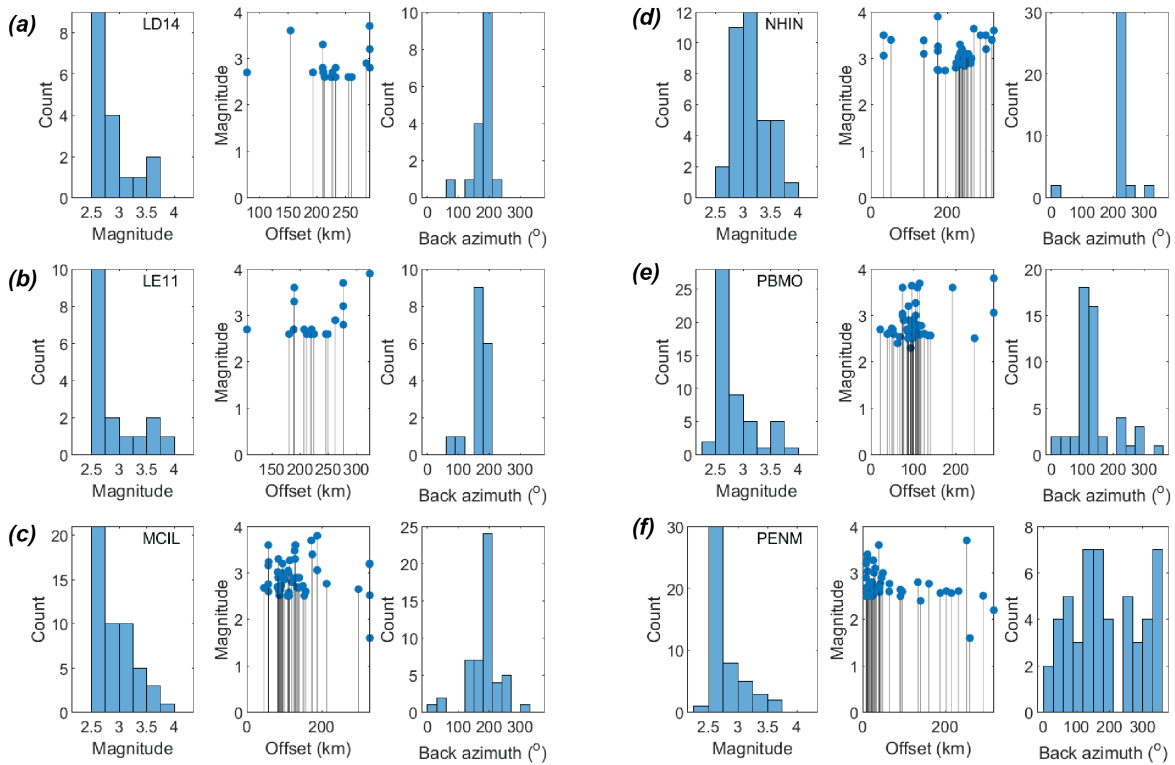


Figure 11. Distributions of earthquakes used to calculate mean S-wave HVSRs at each site: (a) LD14; (b) LE11; (c) MCIL; (d) NHIN; (e) PBMO; (f) PENM.

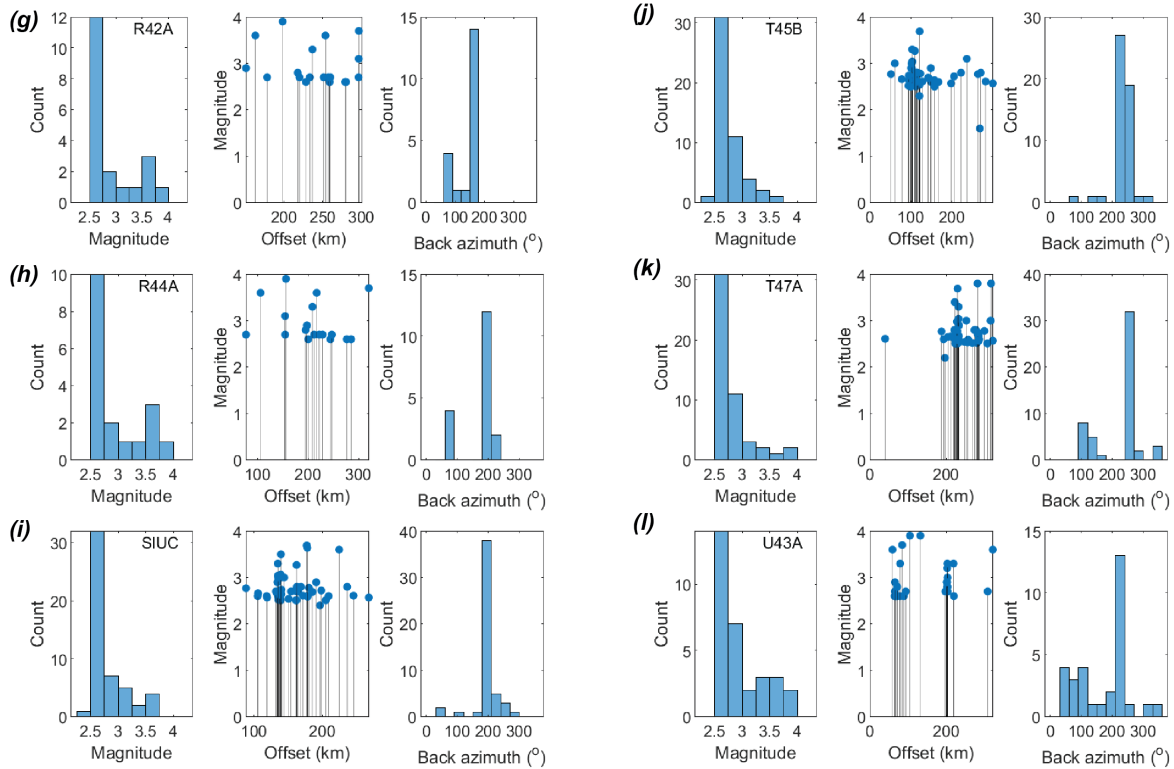


Figure 11, continued. Distributions of earthquakes used to calculate mean S-wave HVSRs at each site: (g) R42A; (h) R44A; (i) SIUC; (j) T45B; (k) T47A; (l) U43A.

Figure 12 shows the mean S-wave HVSR curves developed at each station using the processing parameters listed in Table 3 and the earthquakes shown in Figure 11. The corresponding fundamental-mode frequency and amplification picks are also shown. As illustrated by the modest standard deviations about the mean at each site, the HVSRs are very stable, despite having used amplitude spectra from variety of sources and source-to-site paths. This supports the observations made at other sites (e.g., Lermo and Chávez-García, 1993; Field and Jacob, 1995; Rong et al., 2017; Carpenter et al., 2020) that earthquake HVSR can reveal characteristics of site response.

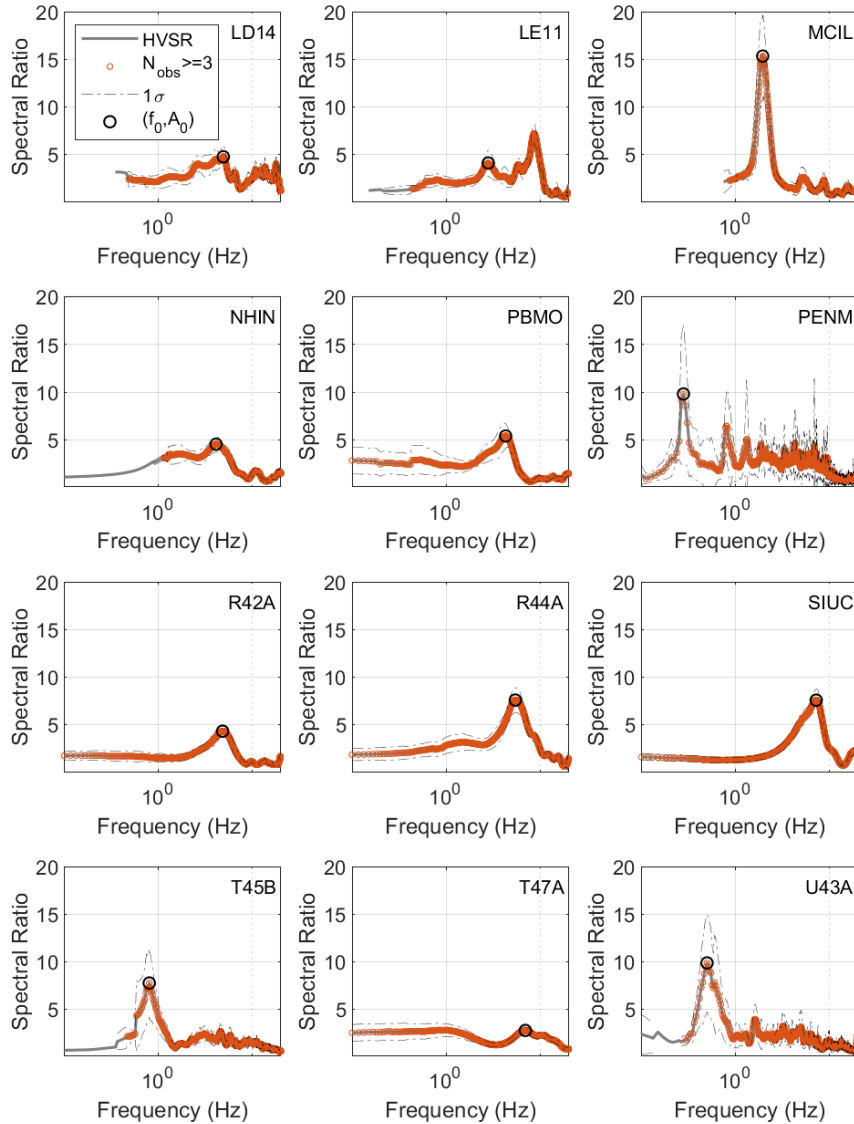


Figure 12. Mean S-wave HVSR curves determined at each site (gray). Mean spectral ratios determined by at least three earthquakes are plotted as orange circles. Mean ± 1 standard deviation are also shown (1σ). Fundamental-mode spectral ratio peaks picked by FINDPEAKS are plotted as black circles.

S-wave velocity structures

Table 4 lists the 1D earth models determined for each station, derived from the reflection/refraction soundings, the $\rho(V_s)$ and $Q_s(V_s)$ relationships, and from the S-wave HVSR inversions. The V_s profiles are also plotted in Figure 13.

Table 4. Sediment and upper-most bedrock S-wave velocity, density, and S-wave quality factor structures derived for the 12 stations. *h* = Inf designates bedrock half-space.

Station	<i>h</i> (m)	<i>V_s</i> (m/s)	ρ (kg/m ³)	<i>Q_s</i>
LD14	5.5	75	1.5	12
	Inf	1313	2.3	83
LE11	11.9	164	1.8	15
	Inf	1615	2.3	106
MCIL	20.5	153	1.7	16
	Inf	2849	2.6	167
NHIN	1.3	81	1.5	12
	18	252	1.9	21
	Inf	1200	2.2	83
PBMO	1.5	175	1.8	17
	23.5	649	2.1	45
	Inf	893	2.2	62
PENM	26	170	1.8	17
	39	317	1.9	25
	43	636	2.1	44
	141	482	2.0	34
	181	510	2.0	36
	128	1038	2.2	69
	Inf	2485	2.5	167
R42A	2.5	320	1.9	25
	Inf	1822	2.4	125
R44A	7	149	1.7	16
	Inf	1287	2.2	85
SIUC	5.8	152	1.7	16
	Inf	1431	2.3	100
T45B	5	165	1.7	17
	35	482	2.0	34
	29	550	2.0	38
	74	460	2.0	33
	Inf	2451	2.5	161
T47A	0.7	122	1.6	14
	3	531	2.0	38
	Inf	924	2.2	62
U43A	25	166	1.8	17
	51	475	2.0	33
	96	361	2.0	28
	Inf	2567	2.5	167

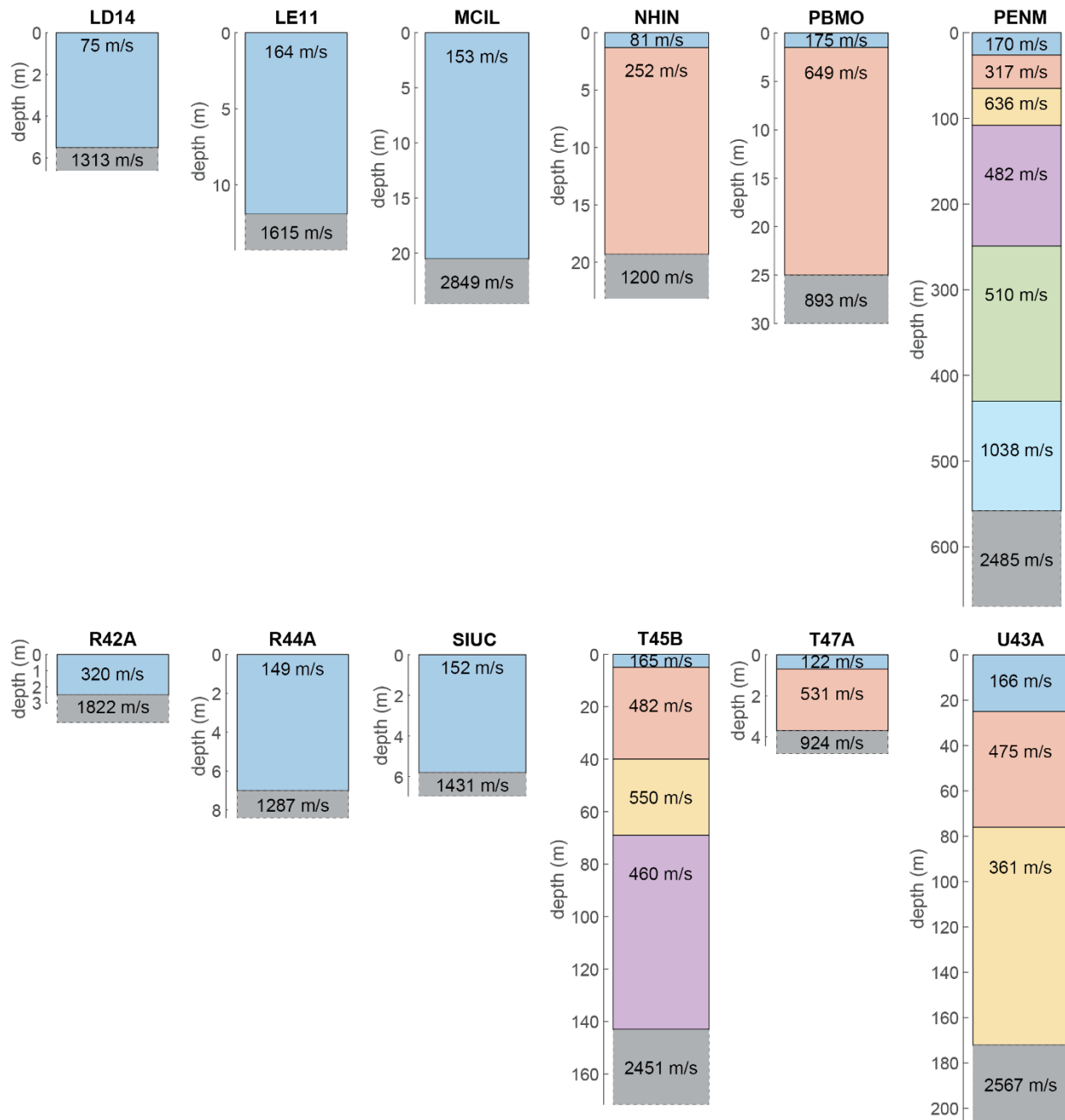


Figure 13. Shear-wave velocity structures developed for this project. The base of each profile represents the greatest depth resolved by the techniques employed. Depth scales differ for each velocity model.

S-wave HVSR modeling for deeper (>100 m) sites

PENM

The near-surface earth model determined for PENM is listed in Table 5. The depth to bedrock, 558 m, was determined through P-wave reflection processing and is consistent with the depth to Paleozoic bedrock for this station of 551 m estimated at this site by Mostafanejad and Langston (2017) using the borehole and seismic data compilation in Dart (1992) and Dart and Swolfs (1998). Figure 14 shows the V_s structures determined through the S-wave eHVSR inversion trials at PENM and a comparison of the

observed HVSR and the HVSR calculated for this station using equation 4 and the best-fitting earth model (Table 5).

Table 5. Near-surface earth model developed for PENM. $h = \text{Inf}$ represents the bedrock half-space.

h (m)	V_p (m/s)	V_s (m/s)	ρ (kg/m ³)	Q_p	Q_s
26	1,245	170	1.8	39	17
39	1,245	317	1.9	63	25
43	1,692	636	2.1	87	44
141	1,711	482	2.0	146	34
181	1,729	510	2.0	116	36
128	3,537	1,038	2.2	319	69
Inf	4,299	2,485	2.5	816	164

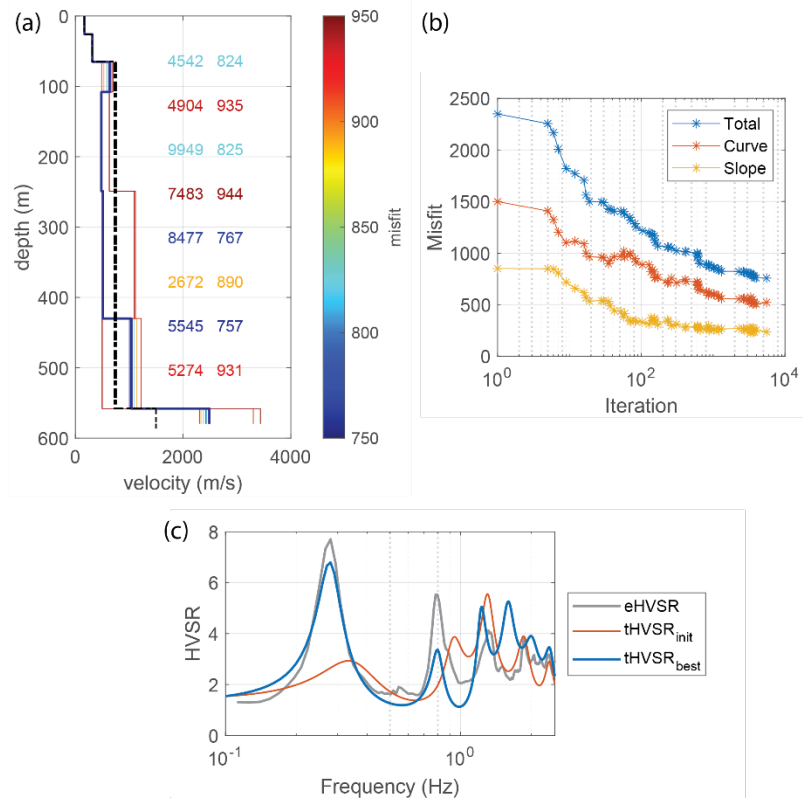


Figure 14. Results from inversion of mean S-wave eHVSr for the S-wave velocity structure at PENM. (a) Starting-S-wave velocity model (black, dashed) and the S-wave velocity structures determined from eight trials, colored by total misfit. (b) Convergence history for the best-fitting trial. The total misfit of the spectral-ratio amplitudes at each frequency (first term in equation 4) (Curve), the total misfit of the slope (second term in equation 4) (Slope), and the sum of the two (Total) are shown. (c) Mean S-wave eHVSr curves observed (eHVSr) and predicted by the best-fitting earth model (Table 5) (tHVSr_{best}). The predicted curve using the starting earth model (tHVSr_{init}) is also shown.

PENM is 29 km from the bedrock-penetrating borehole CUSSO, where both a S-wave velocity model into bedrock and an empirical SH-wave transfer function (eTF) are available (Carpenter et al., 2018a; 2020).

Because the embayment has relatively flat layers (Langston and Horton, 2014) and an approximately 1D site response (Carpenter et al., 2018a) and because PENM and CUSSO have similar sediment-column thicknesses, 558 m and 585 m, respectively, and average sediment V_s , 501 m/s and 546 m/s, respectively, the theoretical, linear SH-wave transfer function derived using the S-wave velocity structure resolved at PENM can be compared with the eTF at CUSSO, as shown in Figure 15. Figure 15 also shows S-wave velocity structures developed by Wood and Himel (2019) using surface wave and microtremor-HVSR techniques at other sites in the embayment overlying thick sediment columns and at CUSSO (Carpenter et al., 2020).

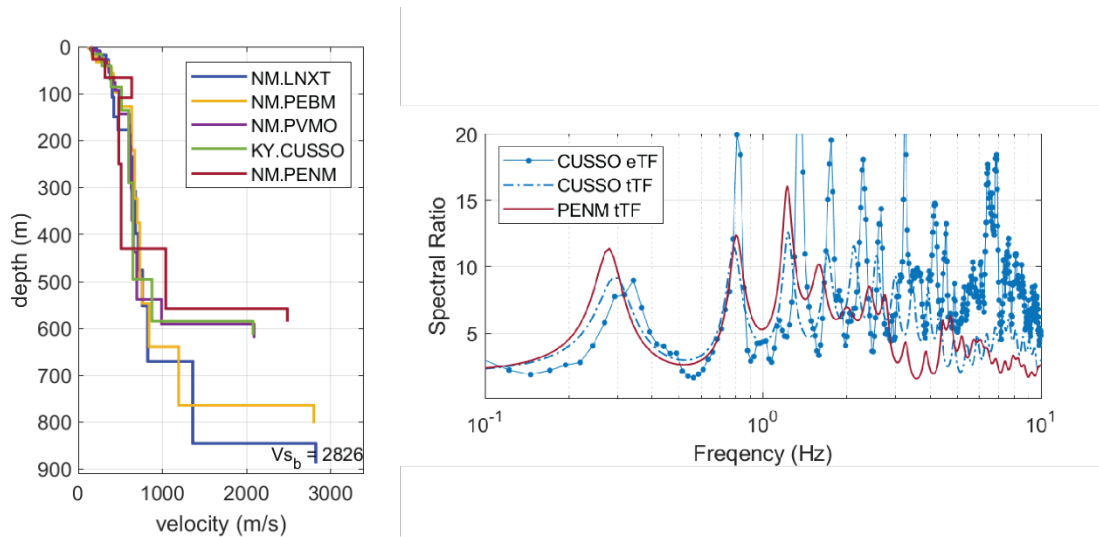


Figure 15. (left) Shear-wave velocity structures at PENM and other nearby, deep-soil sites in the Embayment and the vertical seismic array CUSSO. (right) Empirical (eTF) and theoretical (tTF) weak-motion SH-wave transfer functions at PENM and CUSSO.

The close correspondence between the eTF at CUSSO and the tTF at PENM, particularly at f_0 , suggests that the velocity structure determined at PENM through our techniques is reasonable. This is corroborated by the model at PENM having similar characteristics to those developed at nearby sites. This figure also reiterates that peak amplification may occur at frequencies higher than f_0 in the Embayment.

T45B

The near-surface earth model determined for T45B is listed in Table 6. The depth to bedrock, 143 m, was determined through P-wave reflection processing and is consistent with the depths to Paleozoic bedrock measured at three nearby (within 3 km) sites using surface surveys as reported in Zhu et al. (2021): the depth measurements range from 97 m to 160 m with a mean of 129 m. Figure 16 shows the V_s structures determined through the S-wave eHVSR inversion trials at T45B and a comparison of the observed HVSR and the HVSR calculated for this station using equation 4 and the best-fitting earth model (Table 6).

Table 6. Near-surface earth model developed for T45B. $h = \text{Inf}$ represents the bedrock half-space.

h (m)	V_p (m/s)	V_s (m/s)	ρ (kg/m ³)	Q_p	Q_s
5	1,010	165	1.8	63	17
35	1,010	482	2.0	146	34
29	1,190	550	2.0	178	39
74	1,563	460	2.0	98	33
Inf	4,236	2,435	2.5	527	161

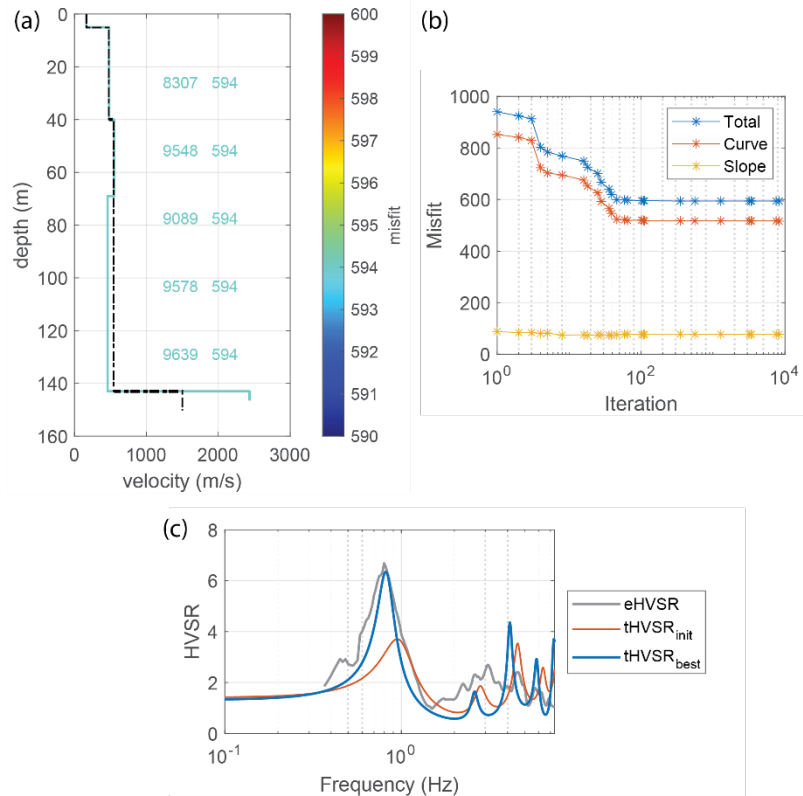


Figure 16. Results from inversion of mean S-wave eHVSr for the S-wave velocity structure at T45B. (a) Starting-S-wave velocity model (black, dashed) and the S-wave velocity structures determined from eight trials, colored by total misfit. (b) Convergence history for the best-fitting trial. The total misfit of the spectral-ratio magnitudes at each frequency (first term in equation 4) (Curve), the total misfit of the slope (second term in equation 4) (Slope), and the sum of the two (Total) are shown. (c) Mean S-wave eHVSr curves observed (eHVSr) and predicted by the best-fitting earth model (Table 6) (tHVSr_{best}). The predicted curve using the starting earth model (tHVSr_{init}) is also shown.

T45B is 20 km from the other bedrock-penetrating borehole in the Embayment, VSAP, where both a S-wave velocity model into bedrock and an empirical SH-wave transfer function (eTF) are also available (Carpenter et al., 2018a). Thus, the theoretical, linear SH-wave transfer function derived using the S-wave velocity structure resolved at T45B can be compared with the eTF at VSAP. However, although these sites are relatively nearby and the average sediment S-wave velocities are similar (VSAP, 392 m/s; T45B, 452 m/s) the depths to bedrock differ by more than 40 percent (VSAP, 100 m; T45B, 143 m). Thus, the comparison is not as straightforward as between CUSSO and PENM. Nevertheless, Figure 17 shows

that the sediment velocities at these sites are similar. The figure also shows that the observed and predicted spectral amplifications are similar at the two sites, but, due to the thicker, low-velocity sediment column at T45B, the resonance frequencies are lower than at VSAP. Finally, this figure provides another example of sites where peak amplification may occur at frequencies higher than f_0 in the Embayment.

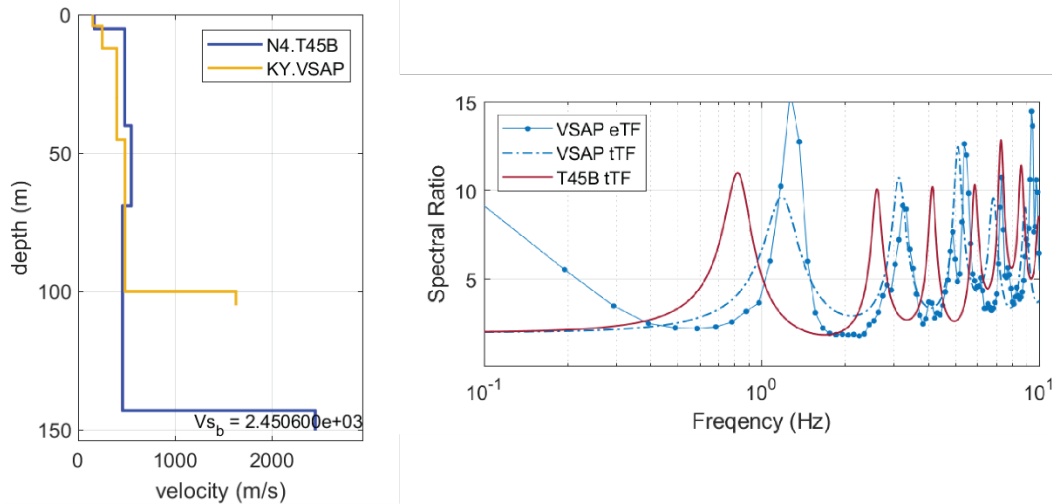


Figure 17. (left) Shear-wave velocity structures at T45B and the vertical seismic array VSAP. (right) Empirical (eTF) and theoretical (tTF) weak-motion SH-wave transfer functions at T45B and VSAP.

U43A

The near-surface earth model determined for U43A is listed in Table 7. The depth to bedrock, 172 m, was determined through P-wave reflection processing and is significantly shallower than the depth to Paleozoic bedrock for this station of 270 m estimated at this site by Mostafanejad and Langston (2017) using the borehole and seismic data compilation in Dart (1992) and Dart and Swolfs (1998). We note, however, that the depth to bedrock estimated in our investigation is consistent with depths in the dataset compiled by Csontos et al. (2008) as shown in Figure 18. In particular, two nearby sites that are similar distances from the Embayment’s edge as U43A have bedrock depths of 175 m and 177 m.

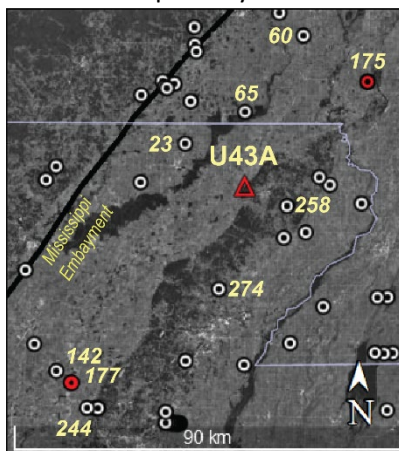


Figure 19 shows the V_s structures determined through the S-wave eHVSr inversion trials at PENM and a comparison of the observed HVSr and the HVSr calculated for this station using equation 4 and the best-fitting earth model (Table 7).

Figure 18. Locations of well- and seismic-based data compiled by Csontos et al. (2008) (white circles) and seismic station U43A (red triangle). The depths-to-bedrock (m) at selected locations are labeled; two wells (red circles) that are similar distances from the edge of the Embayment as is U43A are in red. Refer to Figure 3 for the location of U43A.

Table 7. Near-surface earth model developed for U43A. $h = \text{Inf}$ represents the bedrock half-space.

h (m)	V_p (m/s)	V_s (m/s)	ρ (kg/m ³)	Q_p	Q_s
25	1,315	166	1.8	56	17
51	1,315	475	2.0	106	34
96	1,762	361	2.0	76	27
Inf	4,441	2,567	2.5	1,198	170

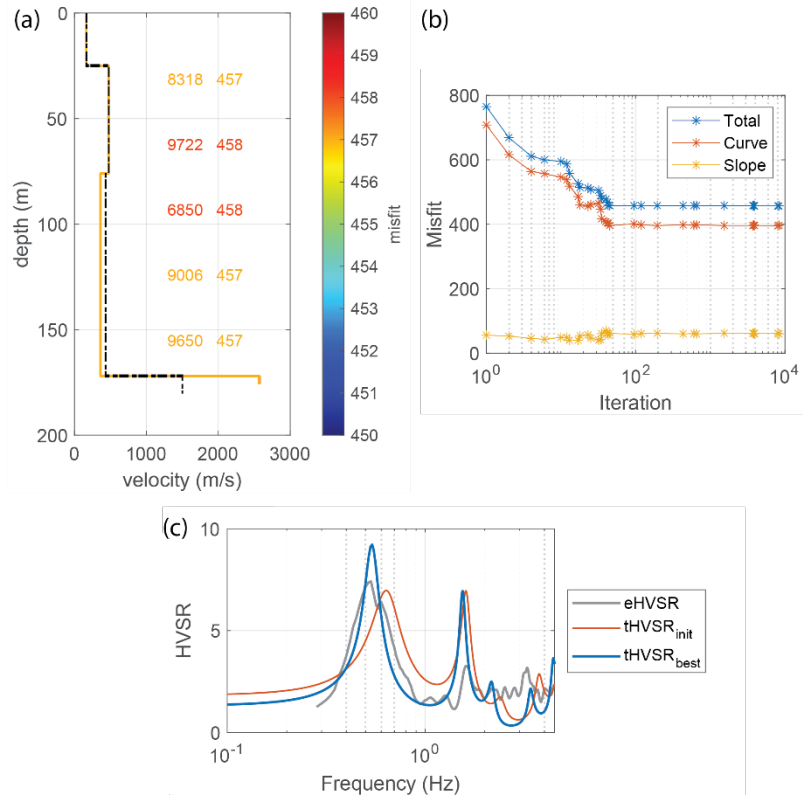


Figure 19. Results from inversion of mean S-wave eHVSr for the S-wave velocity structure at U43A. (a) Starting-S-wave velocity model (black, dashed) and the S-wave velocity structures determined from eight trials, colored by total misfit. (b) Convergence history for the best-fitting trial. The total misfit of the spectral-ratio magnitudes at each frequency (first term in equation 4) (Curve), the total misfit of the slope (second term in equation 4) (Slope), and the sum of the two (Total) are shown. (c) Mean S-wave eHVSr curves observed (eHVSr) and predicted by the best-fitting earth model (Table 7) (tHVSr_{best}). The predicted curve using the starting earth model (tHVSr_{init}) is also shown.

Primary linear site-response parameters

Results of the 1D linear site response modeling are shown in Figure 20 and listed in Table 8. The fundamental-mode frequencies and amplifications, both the first peak in the response curve and the one-sediment-layer-over-bedrock approximations calculated by equations 1 and 2 are also shown and are also listed in Table 8. At R42A and T47A, theoretical f_0 are at frequencies greater than 30 Hz. Within the frequency band of primary engineering interest (i.e. 0.1 Hz to 10 Hz), the maximum amplification occurs at f_0 at all but three sites, namely the thick-soil sites in the Mississippi embayment: PENM, T45B, and U43A. Thus, these results support the findings in recent studies (Carpenter et al., 2020; Zhu et al.,

2021) that the fundamental mode may be considered of primary importance for characterizing linear site response for most sites. However, at thicker-soil sites, determining the peak response may require full 1D site-response calculations. Figure 20 also shows that equations 1 and 2 closely approximate f_0 and A_0 , respectively, determined from 1D linear site-response analysis at most sites. Thus, as observed by Carpenter et al. (2020), the approximations given in equations 1 and 2 are useful to approximate the primary site site-response characteristics at sites where detailed velocity structures are unavailable.

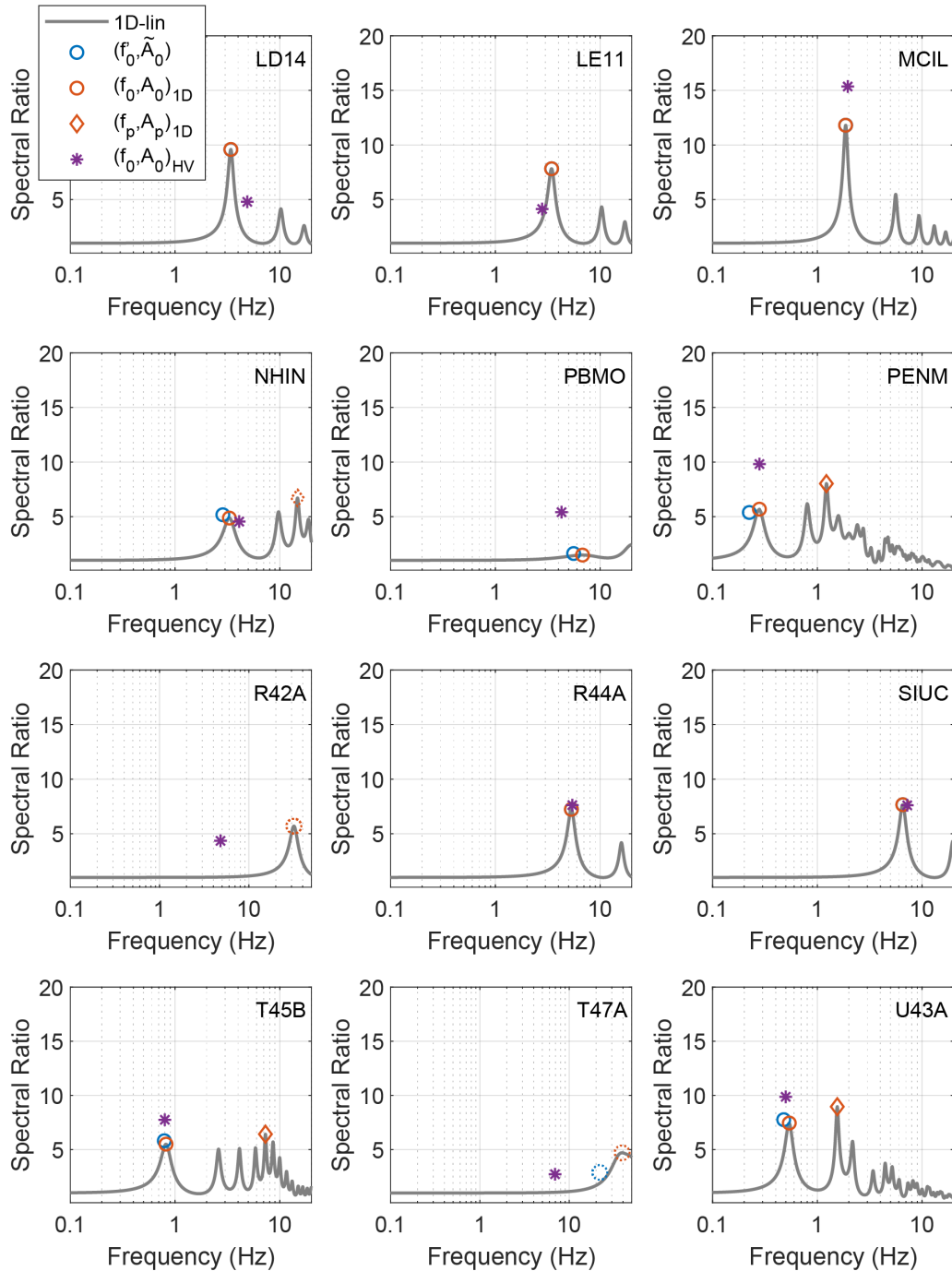


Figure 20. 1D-linear site responses calculated using the velocity structures developed in this study. The first (fundamental mode) peaks are indicated by red circles. Peak amplifications (diamonds) are shown at sites where the maximum amplification occurs at $f > f_0$. Peaks that occur at $f > 10$ Hz are dotted. The one-sediment-layer fundamental-mode parameters calculated by equations 1 (f'_0) and 2 (\tilde{A}_0) and the first peaks measured from the mean S-wave HVSR curves in Figure 12 (HV) are also shown.

Table 8. Fundamental-mode frequency and amplification determined from 1D linear site-response modeling and from the 1-sediment-layer-over-bedrock approximations in equations 1 and 2. Bedrock-sediment impedance ratios are included for comparison.

sta	f_0 (Hz)	A_0	f'_0 (Hz)	\tilde{A}_0	IR
LD14	3.41	9.59	3.41	9.58	27.13
LE11	3.44	7.82	3.45	7.82	13.02
MCIL	1.86	11.8	1.87	11.81	27.79
NHIN	3.3	4.87	2.86	5.17	6.5
PBMO	6.79	1.48	5.58	1.62	1.67
PENM	0.28	5.68	0.22	5.38	6.07
R42A	31.90	5.69	32.00	5.69	6.93
R44A	5.31	7.23	5.32	7.23	11.32
SIUC	6.54	7.66	6.55	7.66	12.45
T45B	0.82	5.5	0.79	5.82	6.75
T47A	39.01	4.70	21.95	2.89	3.14
U43A	0.54	7.45	0.48	7.76	10.08

Recent studies have suggested that site terms can be accounted for using the site-period alone. Our results do not support this, as demonstrated in Figure 21. This figure shows that there is no relationship (coefficient of determination of 0.09 for a linear model) between A_0 and f_0 and equations 1 and 2 provide a physical explanation for this lack of correlation: A_0 depends on both the bedrock and the sediment column whereas f_0 depends on the properties of the sediment column alone.

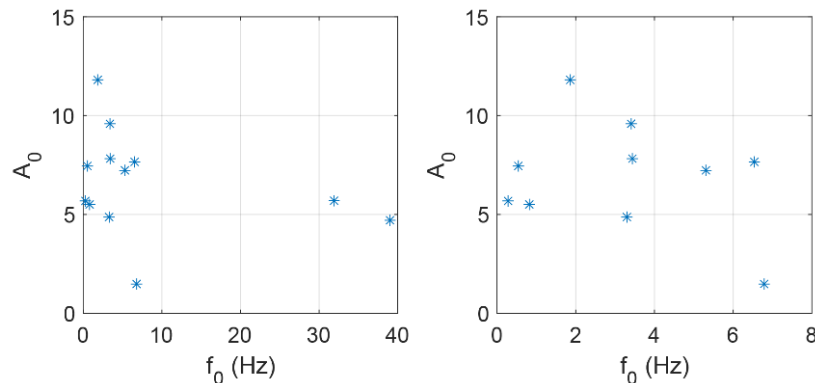


Figure 21. Fundamental-mode amplification vs frequency. The righthand figure shows the same data on a smaller frequency domain.

Figure 22 compares the calculated fundamental-mode response parameters with those measured from the mean S-wave HVSR curves. Predicted and observed f_0 are comparable at all sites except R42A and

T47A, supporting the observations in numerous other studies in this project area and elsewhere that S-wave HVSR can be used to measure fundamental resonance frequencies. At both R42A and T47A, the first HVSR peaks could be due to deeper structure, beneath the base of the sites' velocity profiles, as observed in the Illinois Basin by Carpenter et al. (2020) which would not be captured by our 1D analyses. However, the Nyquist frequencies are too low at both sites to permit analysis at sufficiently high frequencies for reliable comparison with the 1D site response models. Nevertheless, as Figure 22 suggests there is a HVSR peak at high frequency at T47A, consistent with the modeling result. A similar comparison is not possible at R42A because of the much lower Nyquist frequency of 20 Hz. Therefore, the comparisons between HVSR and the modeled responses at these stations may be unreliable.

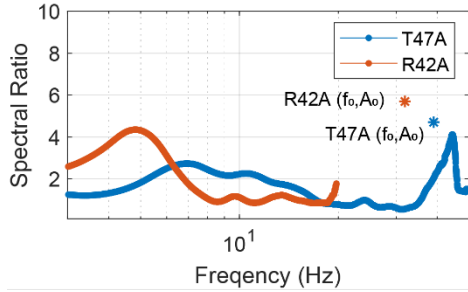


Figure 22. S-wave HVSR curves at T47A and R42A plotted to the corresponding stations' Nyquist frequencies. The fundamental-mode response parameters f_0 and A_0 predicted from 1D linear site response analyses for these sites using the earth models developed in this study are also shown (asterisks).

Although Carpenter et al. (2020) observed a linear relationship between A_0 measured from S-wave HVSR and that predicted from 1D linear analysis, the observations in this study are more scattered and appear uncorrelated. We also observed no relationship between A_0 , measured from S-wave HVSR, and site bedrock-sediment impedance ratios.

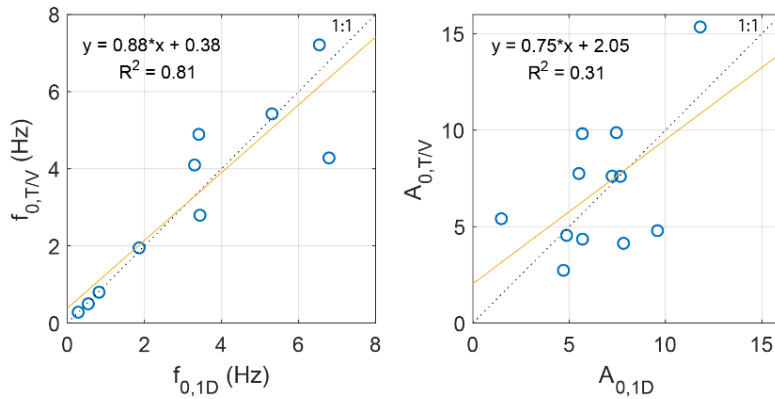


Figure 22. (left) Comparison of f_0 predicted ($f_{0,1D}$) and observed ($f_{0,TV}$)-- R42A and T47A are not shown-- and A_0 predicted ($A_{0,1D}$) and observed ($A_{0,TV}$). Best-fitting linear models to the data shown are plotted (orange); the corresponding equations and coefficients of determination are shown.

Table 8 also lists the bedrock-sediment impedance ratios (IR) for each site. As discussed for equation 2, the sediment impedance is calculated using the time-weighted-average V_s and thickness-weighted-average density for the layers above the bedrock half-space. Figure 23a compares IR with A_0 calculated from the 1D linear analyses and illustrates that IR s less than ~ 5 are consistent with A_0 , but as A_0 increases, IR increasingly overestimates A_0 . As IR approaches 30 (i.e., at LD14 and MCIL), it overestimates A_0 by a factor of ~ 3 . This figure also suggests that there is no clear correspondence between the similarity of A_0 and IR and fundamental frequency (plotted as site-period, i.e., $1/f_0$). Nevertheless, the high coefficient of determination for a power-law fit between IR and A_0 suggests that IR can be used to predict A_0 . Figure 23b illustrates that the A_0 approximation in Equation 2 is consistent

with A_0 determined from 1D linear analysis. Thus, as surmised from equation 2, damping has increasing influence at sites with strong impedance ratios, which corresponds to sites with slower S-wave velocities in the sediment column.

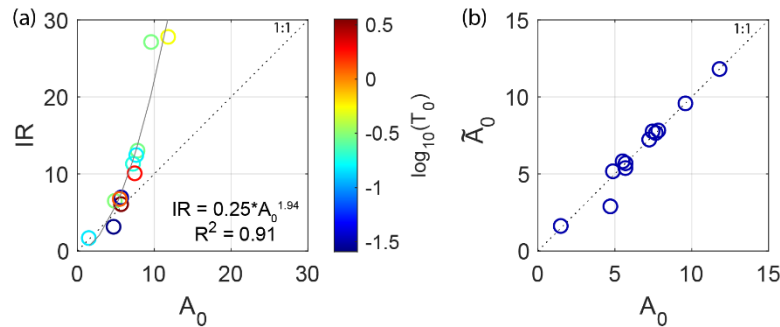


Figure 23. (a) Bedrock-sediment impedance ratios vs A_0 calculated from 1D-linear site response analyses, where the points are colored by T_0 , i.e. $1/f_0$, (left) and by sediment-column thickness Z_{br} . (b) Comparison of A_0 calculated from equation 2 and those determined by the 1D analyses.

1D Equivalent-linear and nonlinear analyses

Tables 8 lists the results of determining the fundamental-mode frequency and corresponding amplification through the 1D equivalent-linear modeling using the near-surface (sediment and uppermost bedrock) earth models developed for these sites. Although we proposed to use 1D nonlinear analysis only for sites with sediment thicknesses of greater than 30 m, we report the results f_0 and A_0 results for all sites in Table 9. Figure 24 compares the 1D strong-motion responses at PENM with the 1D response determined for a generic site with 600m of underlying sediment over bedrock in the Embayment developed in Romero and Rix (2005). The results are comparable, suggesting that the velocity structure developed at PENM and the 1D modeling at that in this study are reasonable. The results are shown in Figures 25 and 26 along with results from linear modeling and from the S-wave HVSR observations. We proposed to use empirical transfer functions from VSAP and CUSSO to compare with the equivalent-linear and nonlinear analyses but lacked recording strong-motions to do so. Thus, our comparisons between modeled and observed SH-wave transfer functions are restricted to the weak-motion comparisons shown in Figures 15 and 17. We were also unable to compare empirical site responses at the borehole along the Ohio River, HEKY (Figure 2), because we determined that downgoing waves too strongly contaminate the bedrock recordings, rendering peak values measured from the spectral ratios as unusable.

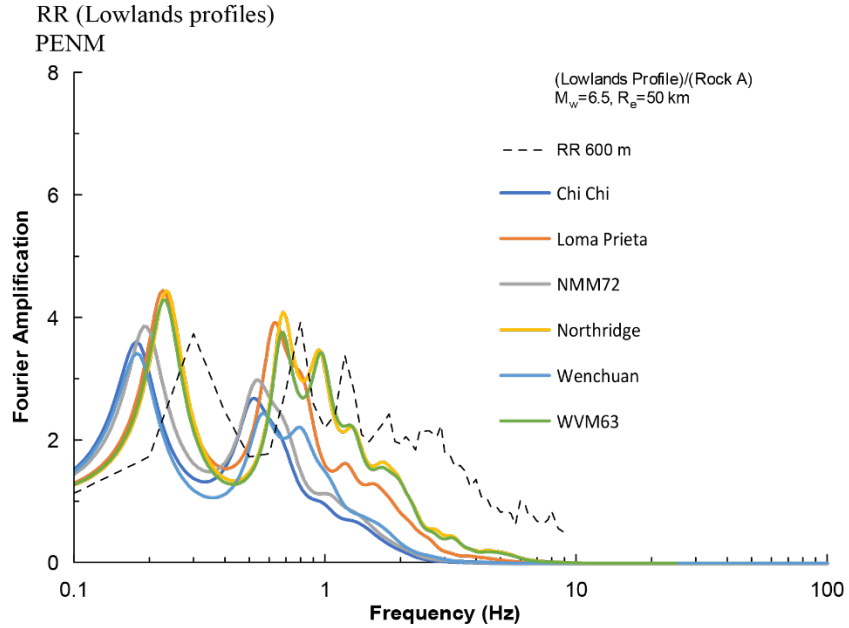


Figure 24. Comparison of 1D equivalent-linear responses determined at PENM with the 1D response determined at a generic embayment site with 600 m of underlying sediment in Romero and Rix (2005). Modified from Romero and Rix (2005)

Table 8. Fundamental-mode frequency and amplification determined from 1D Equivalent-linear modeling using six ground-motion time-histories.

Site	Chi Chi (0.18g)		Loma Prieta (0.17g)		Northridge (0.10g)		Wenchuan (0.42g)		NMM72 (0.43g)		WVM63 (0.17g)	
	f_0 (Hz)	A_0	f_0 (Hz)	A_0	f_0 (Hz)	A_0	f_0 (Hz)	A_0	f_0 (Hz)	A_0	f_0 (Hz)	A_0
LD14	1.15	2.9	1.32	3.08	1.59	3.4	0.96	2.75	0.89	2.71	1.76	3.68
LE11	1.65	3.26	1.95	3.7	2.06	3.83	1.48	3.07	1.33	2.94	2.3	4.19
MCIL	0.65	2.94	0.9	3.51	1.12	4.24	0.81	3.26	0.68	2.99	1.17	4.41
NHIN	1.92	3.19	2.27	3.46	2.42	3.63	1.66	3.01	1.63	2.98	2.47	3.7
PBMO	5.95	1.48	5.9	1.49	6.28	1.48	5.36	1.51	5.30	1.52	5.93	1.49
PENM	0.18	3.93	0.23	5.21	0.23	5.26	0.17	3.67	0.19	4.24	0.23	5.03
R42A	30.85	5.76	30.92	5.8	31.38	6.12	29.72	5.19	-	-	-	-
R44A	3.4	3.91	3.13	3.69	4.02	4.68	1.93	2.84	2.07	2.91	3.16	3.72
SIUC	4.75	4.56	3.64	3.64	5.24	5.28	2.26	2.81	2.55	2.94	3.65	3.64
T45B	0.44	2.9	0.57	3.41	0.67	4.02	0.46	3.01	0.48	3.05	0.67	4.03
T47A	36.81	5.02	36.96	5.02	37.82	5.15	34.16	4.85	-	-	-	-
U43A	0.27	3.01	0.4	3.77	0.43	4.06	0.31	3.16	0.35	3.67	0.43	3.93

Table 9. Fundamental-mode frequency and amplification determined from 1D nonlinear modeling using six ground-motion time-histories.

Site	Chi Chi (0.18g)		Loma Prieta (0.17g)		Northridge (0.10g)		Wenchuan (0.42g)		NMM72 (0.43g)		WVM63 (0.17g)	
	f_0 (Hz)	A_0	f_0 (Hz)	A_0	f_0 (Hz)	A_0	f_0 (Hz)	A_0	f_0 (Hz)	A_0	f_0 (Hz)	A_0
LD14	1.46	3.18	1.39	4.89	1.86	6.27	1.12	2.59	1.86	3.01	2.03	4.03
LE11	2.07	4.57	2.32	6.48	1.93	5.55	1.43	2.74	1.96	4.28	2.41	4.93
MCIL	1.08	3.02	1.39	5.79	1.35	6.11	0.94	3.21	0.89	2.74	1.29	3.79
NHIN	2.11	4.22	2.31	5.59	2.56	5.04	2.44	2.62	1.96	4.1	2.41	4.6
PBMO	5.98	2.09	5.84	2.02	5.9	1.98	5.44	2.18	5.54	2.91	6.01	2.8
PENM	0.15	2.61	0.23	3.54	0.23	3.03	0.2	2.59	0.21	4.08	0.2	3
R42A	27.51	9.58	27.61	12.03	27.23	7.58	28.06	8.55	-	-	-	-
R44A	4.44	5.2	3.15	3.58	4.43	6.22	2.44	3.22	2.98	4.66	2.97	3.92
SIUC	5.1	10.08	4.82	5.07	5.42	12.53	3.44	3.83	3.12	3.36	5.24	7.34
T45B	0.49	2.77	0.52	3.41	0.69	3.67	0.45	3.04	0.49	6.09	0.65	3.64
T47A	30.9	7.13	31.92	7.17	30.23	5.02	29.52	11.83	-	-	-	-
U43A	0.25	2.26	0.38	3.19	0.41	3.13	0.34	2.63	0.35	3.42	0.43	2.6

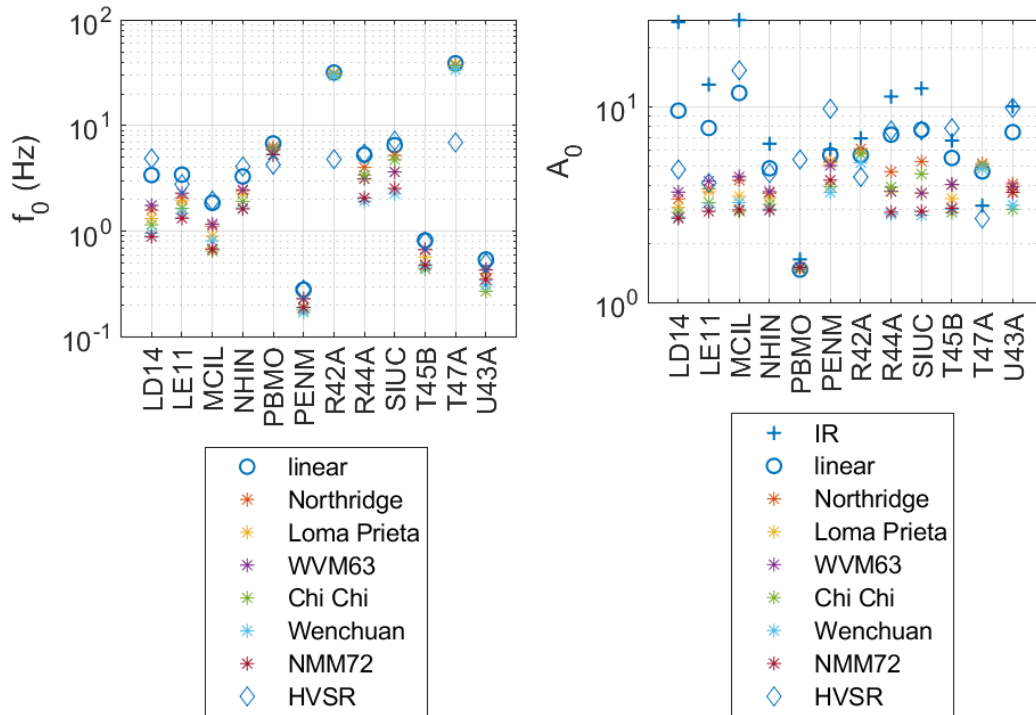


Figure 25. Results of linear and equivalent-linear 1D site response modeling and measurements from S-wave HVSr. Bedrock-sediment impedance ratios are also shown.

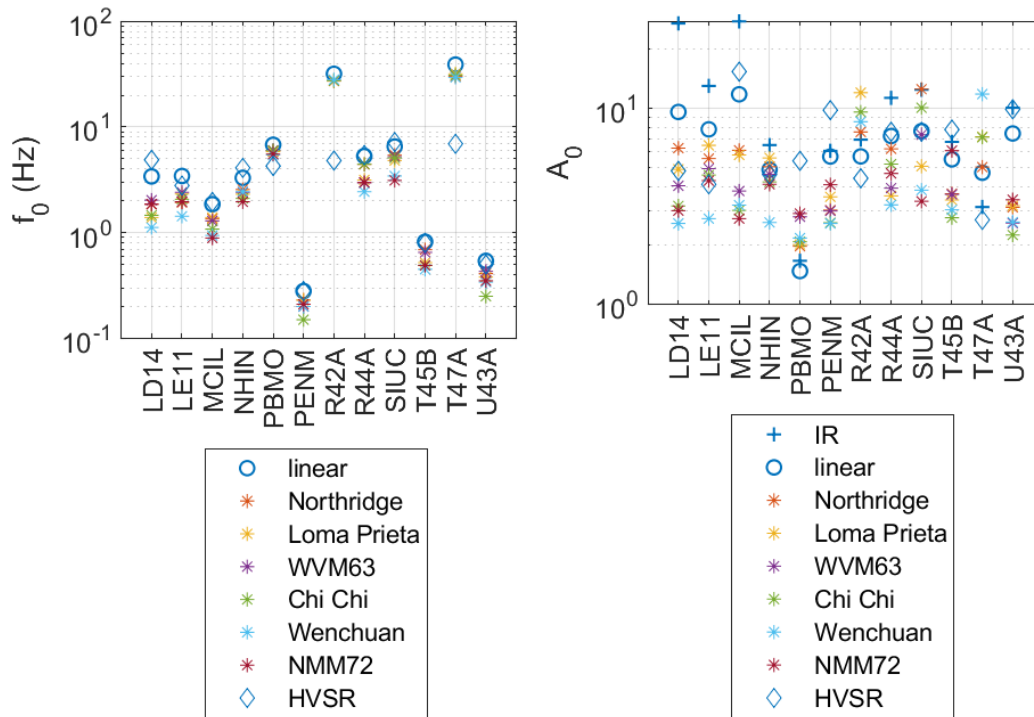


Figure 26. Results of linear and nonlinear 1D site response modeling and measurements from S-wave HVSR. Bedrock-sediment impedance ratios are also shown.

The 1D equivalent-linear and nonlinear modeling results show that f_0 tends to decrease with increasing PGA. Thus, f_0 measured from weak-motion S-wave HVSR, such as those observed in this study, may increasingly overestimate the site's fundamental frequency as ground motion intensities increase. For equivalent-linear modeling, as ground motion increases, A_0 also tends to decrease. However, 1D nonlinear modeling does not consistently demonstrate the same affect on A_0 . For example, at certain sites such as R42A and SIUC, the nonlinear response simulations yield amplifications that are larger than those determined through linear site-response modeling. There is no clear relationship between A_0 measured from HVSR and that determined through the 1D nonlinear modeling. Finally, as expected from Figure 23, bedrock-sediment impedance ratios provide a weaker estimation of strong-motion A_0 determined from equivalent-linear analysis than that which results from the linear modeling. There is no clear relationship between IR and A_0 determined from nonlinear analysis.

Conclusions

In this project, we evaluated the skill of site fundamental frequency, f_0 , the corresponding amplification, A_0 , and sediment-bedrock impedance ratio (IR) to characterize the primary characteristics of site responses at 12 seismic stations in the New Madrid (NMSZ) and Wabash Valley (WVSZ) seismic zones. The IR , A_0 and f_0 parameters were calculated from shear-wave velocity (V_s) profiles developed at each site using 1D linear and equivalent-linear and nonlinear site response analyses and one-layer-over-bedrock approximations. V_s profiles were developed at each site from surface SH-wave reflection/refraction soundings. For the thicker-soil sites (sediment column thickness > 100 m), we estimated the deeper V_s by inversion of earthquake HVSR curves using constrains determined from P-

wave and SH-wave soundings. We also measured the A_0 and f_0 parameters from S-wave HVSR curves that we developed at each site.

Our results support the findings of other recent studies that the primary linear site-response characteristics needed for engineering purposes can be quantified by the A_0 and f_0 parameters at most sites. A corollary of this result is that the pair of parameters--both A_0 and f_0 --is needed to account for site resonance, and a single parameter alone, e.g. f_0 , is insufficient. For sites over thick soil deposits, a linear site-response calculation may be needed because the largest amplifications are predicted to occur at frequencies greater than f_0 . We also found that A_0 and f_0 can be reliably estimated by simplified expressions for one-layer-over-bedrock scenarios. Our observations also support the observations made in our study area and elsewhere that S-wave HVSR can be used to measure linear f_0 . However, we found no clear relationship between the amplitude of the HVSR peak at f_0 and that predicted by linear, equivalent-linear, and nonlinear 1D site responses. Furthermore, we determined that the bedrock-sediment impedance ratio can be used to estimate A_0 through a power-law relationship. Further, through the equivalent-linear and nonlinear modeling, consistent with other studies we found that theoretical f_0 decreases with increasing peak ground-motion amplitudes. Thus, the utility of weak-motion HVSR to predict f_0 in cases of strong motion is limited.

References

- Beyreuther, M., Barsch, R., Krischer, L., Megies, T., Behr, Y. and Wassermann, J., 2010. ObsPy: A Python toolbox for seismology. *Seismological Research Letters*, 81(3), pp.530-533.
- Bignardi, S., Mantovani, A. and Zeid, N.A., 2016. OpenHVSR: imaging the subsurface 2D/3D elastic properties through multiple HVSR modeling and inversion. *Computers & Geosciences*, 93, pp.103-113.
- Bonilla, M.G., 1991, *The Marina District, San Francisco, California: geology, history, and earthquake effects*, *Bulletin of the Seismological Society of America*, 81, pp.1958–1979.
- Boore, D.M., 2016. Determining generic velocity and density models for crustal amplification calculations, with an update of the Boore and Joyner (1997) generic site amplification for $V_S(Z)=760\text{m/s}$. *Bulletin of the Seismological Society of America*, 106(1), pp.313–317.
- Cadet, H., Bard, P.Y. and Rodriguez-Marek, A., 2010. Defining a standard rock site: Propositions based on the KiK-net database. *Bulletin of the Seismological Society of America*, 100(1), pp.172-195.
- Campbell, K.W., 2009. Estimates of shear-wave Q and κ_0 for unconsolidated and semiconsolidated sediments in eastern North America. *Bulletin of the Seismological Society of America*, 99(4), p. 2365–2392.
- Carpenter, N.S., Wang, Z., Woolery, E.W. and Rong, M., 2018. Estimating site response with recordings from deep boreholes and HVSR: Examples from the Mississippi embayment of the central United States. *Bulletin of the Seismological Society of America*, 108(3A), pp.1199-1209.
- Carpenter, N.S., Wang, Z., Woolery, E.W., 2018b. Inversion of Single-Station S-Wave HVSR for Shallow Velocity Structure: Utility and Limitations, Abstract S23C-0537 presented at 2018 AGU Fall Meeting, Washington, D.C., 10-14 Dec.
- Carpenter, N.S., Wang, Z., and E.W. Woolery, 2019, Resolving S-Wave Velocity Structure from Weak-Motion S-Wave HVSR. *Seismological Society of America*, 2019 Annual Meeting, April 23-26, Seattle, Wa.

Carpenter, N.S., Wang, Z., and Woolery, E.W., 2020. An Evaluation of Linear Site-Response Parameters in the Central and Eastern United States and the Importance of Empirical Site-Response Estimations. *Bulletin of the Seismological Society of America*, 110(2), pp.489-507.

Chambers, D.J., Boltz, M.S. and Chamberlain, C.J., 2021. ObsPlus: A Pandas-centric ObsPy expansion pack. *Journal of open source software*, 6(60), p.2696.

Csontos, R., Van Arsdale, R., Cox, R. and Waldron, B., 2008. Reelfoot rift and its impact on Quaternary deformation in the central Mississippi River valley. *Geosphere*, 4(1), pp.145-158.

Dart, R.L., 1992. Catalog of pre-Cretaceous geologic drill-hole data from the upper Mississippi Embayment: A revision and update of open-file report 90-260, U.S. Geological Survey Open-File Rept. 92-685.

Dart, R.L., and Swolfs, H.S., 1998. Contour mapping of relic structures in the Precambrian basement of the Reelfoot Rift, North American midcontinent, *Tectonics*, 17, pp.235–249.

Dix, C. H. (1955). Seismic velocities from surface measurements: *Geophysics* 20, p. 68–86.

Dobry, R., Borcherdt, R.D., Crouse, C.B., Idriss, I.M., Joyner, W.B., Martin, G.R., Power, M.S., Rinne, E.E., and Seed, R.B., 2000, New site coefficients and site classification system used in recent building seismic code provisions, *Earthquake Spectra*, 16, pp.41–67.

Field, E.H. and Jacob, K.H., 1995. A comparison and test of various site-response estimation techniques, including three that are not reference-site dependent. *Bulletin of the seismological society of America*, 85(4), pp.1127-1143.

Geometrics, 2009, *SeisImager/2D™ Manual (V 3.3)*, 257p.

Goulet, C.A., Bozorgnia, Y., Kuehn, N., Atik, L.A., Youngs, R.R., Graves, R.W., and Atkinson, G.M., 2017, NGA-east ground-motion models for the U.S. Geological Survey National Seismic Hazard Maps, PEER Report No. 2017/03, Pacific Earthquake Engineering Research Center, University of California, Berkeley, 180 p.

Hashash, Y.M.A., Musgrove, M.I., Harmon, J.A., Okan, I., Xing, G., Numanoglu, O., Groholski, D.R., Phillips, C.A., and Park, D. (2020) "DEEPSOIL 7.0, User Manual". Urbana, IL, Board of Trustees of University of Illinois at Urbana-Champaign.

Hashash, Y.M., Harmon, J.A., Ilhan, O., Parker, G.A., and Stewart, J.P, 2017, Recommendation for ergodic nonlinear site amplification in central and eastern North America, PEER Report No. 2017/05, Pacific Earthquake Engineering Research Center, University of California, Berkeley, 62 p.

Haskell, N. A. (1960). Crustal reflection of plane SH waves, *J. Geophys. Res.* 65, no. 12, pp.4147–4150.

Hassani, B. and Atkinson, G.M., 2016, Applicability of the NGA-West2 Site-Effects Model for Central and Eastern North America. *Bulletin of the Seismological Society of America*, 106: 653-664.

Hassani, B. and Atkinson, G.M., 2017, Site-Effects Model for Central and Eastern North America Based on Peak Frequency and Average Shear-Wave Velocity. *Bulletin of the Seismological Society of America*, 08 (1): 338–350. doi: <https://doi.org/10.1785/0120170061>.

Idriss, I.M., and Sun, J.I., 1992, SHAKE91: A computer program for conducting equivalent linear seismic response analyses of horizontally layered soil deposits. Center for Geotech. Modeling, Univ. of Calif., Davis.

Kawase, H., Sánchez-Sesma, F.J. and Matsushima, S., 2011. The optimal use of horizontal-to-vertical spectral ratios of earthquake motions for velocity inversions based on diffuse-field theory for plane waves. *Bulletin of the Seismological Society of America*, 101(5), pp.2001-2014.

Konno, K. and Ohmachi, T., 1998. Ground-motion characteristics estimated from spectral ratio between horizontal and vertical components of microtremor. *Bulletin of the Seismological Society of America*, 88(1), pp.228-241.

Kottke, A.R., and Rathje, E.M., 2008. Technical manual for strata. University of California–Berkeley, Pacific Earthquake Engineering Research Center, PEER Report 2008/10, 103 p.

Langston, C.A., 2003. Local earthquake wave propagation through Mississippi embayment sediments, part I: Body-wave phases and local site responses. *Bulletin of the seismological society of America*, 93(6), pp.2664-2684.

Langston, C.A. and Horton, S.P., 2014. Three-dimensional seismic-velocity model for the unconsolidated Mississippi embayment sediments from H/V ambient noise measurements. *Bulletin of the Seismological Society of America*, 104(5), pp.2349-2358.

Lermo, J. and Chávez-García, F.J., 1993. Site effect evaluation using spectral ratios with only one station. *Bulletin of the seismological society of America*, 83(5), pp.1574-1594.

Matsushima, S., Hirokawa, T., De Martin, F., Kawase, H. and Sánchez-Sesma, F.J., 2014. The effect of lateral heterogeneity on horizontal-to-vertical spectral ratio of microtremors inferred from observation and synthetics. *Bulletin of the Seismological Society of America*, 104(1), pp.381-393.

Mostafanejad, A. and Langston, C.A., 2017. Velocity structure of the northern Mississippi Embayment sediments, Part II: Inversion of teleseismic P-wave transfer functions. *Bulletin of the Seismological Society of America*, 107(1), pp.106-116.

Nagashima, F., Matsushima, S., Kawase, H., Sánchez-Sesma, F.J., Hayakawa, T., Satoh, T., and Oshima, M., 2014, Application of horizontal-to-vertical spectral ratios of earthquake ground motions to identify subsurface structures at and around the K-NET site in Tohoku, Japan, *Bulletin of the Seismological Society of America*, 104: 2288–2302.

Peng, Y., Wang, Z., Woolery, E.W., Lyu, Y., Carpenter, N.S., Fang, Y. and Huang, S., 2020. Ground-motion site effect in the Beijing metropolitan area. *Engineering Geology*, 266, p.105395.

Romero, S.M. and Rix, G.J., 2005. Ground motion amplification of soils in the upper Mississippi embayment. MAE Center CD Release 05-01.

Rong, M., Wang, Z., Woolery, E.W., Lyu, Y., Li, X. and Li, S., 2016, Nonlinear site response from the strong ground-motion recordings in western China. *Soil Dynamics and Earthquake Engineering*, 82: 99-110

Seed, H.B., Romo, M.P., Sun, J.I., Jaime, A., and Lysmer, J., 1988, The Mexico earthquake of September 19,1985 – Relationship between soil conditions and earthquake ground motions, *Earthquake Spectra*, 4: 687–729.

SESAME Project, 2004. Guidelines for the Implementation of the H/V Spectral Ratio Technique on Ambient Vibrations. Measurements, Processing and Interpretation. SESAME European Research Project WP12-Deliverable D23-12.

Stewart, J.P, Parker, G.A., Harmon, J.A., Atkinson, G.M., Boore, D.M., Darragh, R.B., Silva, W.J., and Hashash, Y.M., 2017, Expert panel recommendations for ergodic site amplification in central and eastern North America, PEER Report No. 2017/05, Pacific Earthquake Engineering Research Center, University of California, Berkeley, 66 p.

Street, R., Wang, Z., Woolery, E., Hunt, J., and Harris, J., 1997b, Site effects at a vertical accelerometer array near Paducah, Kentucky, *Engineering Geology*, 46, pp.349–367.

Street, R., Woolery, E., Wang, Z., and Harris, J., 2001, NEHRP Soil Classifications for Estimating Site-Dependent Seismic Coefficients in the Upper Mississippi Embayment, *Engineering Geology*, 62: 123–135.

Street, R., Woolery, E.W., and Chiu, J., 2004, Shear-wave velocities of the post-Paleozoic sediments across the Upper Mississippi Embayment, *Seismological Research Letters*, 75: 390–405.

Thompson, E.M., Baise, L.G., Tanaka, Y. and Kayen, R.E., 2012. A taxonomy of site response complexity. *Soil Dynamics and Earthquake Engineering*, 41, pp.32-43.

Wang, Z., Street, R., Woolery, E., and Harris, J., 1994. Qs estimation for unconsolidated sediments using first-arrival SH wave critical refractions. *Journal of Geophysical Research: Solid Earth*, 99(B7), pp.13,543-13,551.

Williams, R.A., Stephenson, W.J., Frankel, A.D., Cranswick, E., Meremonte, M.E. and Odum, J.K., 2000. Correlation of 1-to 10-Hz earthquake resonances with surface measurements of S-wave reflections and refractions in the upper 50 m. *Bulletin of the Seismological Society of America*, 90(5): 1323-1331.

Williams, R.A., Wood, S., Stephenson, W.J., Odum, J.K., Meremonte, M.E., and Street, R., 2003. Surface Seismic–refraction/reflection measurement determinations of Potential Site Resonances and the Areal uniformity of NEHRP Site Class D in Memphis, Tennessee, *Earthquake Spectra*, 19: 159-189.

Wood, C., Himel, A.K., 2019. Development of Deep Shear Wave Velocity Profiles at Seismic Stations in the Mississippi Embayment, Final Technical Report, USGS NEHRP Award G18AP00078, 150 p.

Woolery, E., and Z. Wang (2010). Toward construction of the Central United States Seismic Observatory and Calibration Site: Defining the geologic site model, U.S. Geol. Surv. National Earthquake Hazards Reduction Program Final Technical Rept. 08HQGR0094, 33 pp.

Woolery, E.W., Lin, T., Wang, Z., and Shi, B., 2008, The role of local soil-induced amplification in the 27 July 1980 northeastern Kentucky earthquake, *Environmental & Engineering Geoscience*, 14: 267–280.

Woolery, E., Street, R. and Hart, P., 2009. Evaluation of linear site-response methods for estimating higher-frequency (> 2 Hz) ground motions in the lower Wabash River valley of the central United States. *Seismological Research Letters*, 80(3), pp.525-538.

Woolery, E.W., Street, R, Hart, P., and Padgett, P., 2012, Two decades of linear site-effect observation (>2 Hz) in the Wabash Valley, central United States—Context for the 2008 Illinois earthquake sequence, *Seismological Research Letters*, 83: 1090–1103.

Woolery, E.W., Wang, Z., Seth Carpenter, N., Street, R. and Brengman, C., 2016. The central United States seismic observatory: Site characterization, instrumentation, and recordings. *Seismological Research Letters*, 87(1), pp.215-228.

Zhu, Y., Wang, Z., Carpenter, N.S., Woolery, E.W. and Haneberg, W.C., 2021. Mapping Fundamental-Mode Site Periods and Amplifications from Thick Sediments: An Example from the Jackson Purchase Region of Western Kentucky, Central United States. *Bulletin of the Seismological Society of America*, 111 (4), pp.1868–1884. doi: doi.org/10.1785/0120200300

Project Data

The linear, equivalent-linear, and nonlinear 1D site response functions developed as part of this project are available for download at https://kgs.uky.edu/kygeode/download/NEHRP2020_data.zip. The S-wave HVSR curves developed in this study are also available at that same website. Vertical seismic arrays VSAP and CUSSO are part of the Kentucky Seismic and Strong Motion Network (Kentucky Geological Survey/Univ. of Kentucky (1982): Kentucky Seismic and Strong Motion Network. University of Kentucky. Other/Seismic Network. doi:10.7914/SN/KY), operated by the University of Kentucky. Recordings from these arrays are available for download from <http://www.uky.edu/KGS/geologichazards/data.htm>.

Bibliography

[Related abstracts developed during this project period include:](#)

Wang, Z and Carpenter, N.S., 2021. Primary Linear Site Response Parameters From Transfer Functions and Ratios of Response Spectra, *Seismological Research Letters* April 01, 2021, 92 (2B), p. 1373-1374. doi:<https://doi.org/10.1785/0220210025>.

Carpenter, N.S., Wang, Z., Zhu, Y., Woolery, E.W., 2021. Should Site Response Be Incorporated Into Central U.S. Hazard Maps? *Seismological Research Letters* April 01, 2021, 92 (2B), p. 1453. doi:<https://doi.org/10.1785/0220210025>.

Carpenter, N.S., Yassminh, R., Hickman, J.B., Wang, Z., Site Response in the Illinois Basin From S-wave H/V and Spectral-Element Modeling. *Seismological Research Letters* April 01, 2021, 92 (2B), p. 1308. doi:<https://doi.org/10.1785/0220210025>.

Carpenter, N.S., Yassminh, R., Hickman, J.B., Wang, Z., Site Response from Deep Stratigraphic Layers in the Illinois Basin from S-wave H/V Observations and Spectral-Element Modeling, AGU 2020 Fall Meeting, December 1-17, 2020, Virtual.

Wang, Z., Carpenter, N.S., Assessing Primary Ground-Motion Site-Response Parameters from Borehole-Array Records, AGU 2020 Fall Meeting, December 1-17, 2020, Virtual

Carpenter, N.S., Wang, Z., Woolery, E.W., Can Proxies Adequately Approximate Site Resonance?, 2020 Eastern Section of the Seismological Society of America Annual Meeting Program and Abstracts, 71 p.

Wang, Z., Carpenter, N.S., Woolery, E.W., Kalinski, M.E., New Site Correction Factors and Design Response Spectrum: Their Applications in the Central United States, 2020 Eastern Section of the Seismological Society of America Annual Meeting Program and Abstracts, 71 p.

Carpenter, N.S., Wang, Z., Woolery, E.W., 2020. Should Site Response Be Incorporated into Central and Eastern US Hazard Maps?, *Seismological Research Letters*, 91 (2B), p. 1238, doi: <https://doi.org/10.1785/0220200043>.

Wang, Z., Carpenter, N.S., Woolery, E.W., Kalinski, M.E., 2020 Ground-Motion Site Response and New Physics-Based Site Correction Factors for Design Response Spectrum, *Seismological Research Letters*, 91 (2B), p. 1268, doi: <https://doi.org/10.1785/0220200043>.

Zhu, Y., Wang, Z., Carpenter, N.S., Woolery, E.W., Haneberg, W.C., 2020. Fundamental Site Period and Peak Amplification Maps for the Jackson Purchase Region in the New Madrid Seismic Zone, *Seismological Research Letters*, 91 (2B), p. 1276, doi: <https://doi.org/10.1785/0220200043>.

[Journal publications include:](#)

Zhu, Y., Wang, Z., Carpenter, N.S., Woolery, E.W., and Haneberg, W.C., 2021. Mapping Fundamental Site Periods and Corresponding Amplifications for the Jackson Purchase Region of Western Kentucky, Central United States, *Bulletin of the Seismological Society of America*. 111 (4), p. 1868–1884, doi: [10.1785/0120200300](https://doi.org/10.1785/0120200300)